Numerical simulations of black hole-neutron star mergers in scalar-tensor gravity

Sizheng Ma,[1,*] Vijay Varma,[2,3,4,5,†] Leo C. Stein,[6] Francois Foucart,[7] Matthew D. Duez,[8] Lawrence E. Kidder,[4] Harald P. Pfeiffer,[2] and Mark A. Scheel[1]

[1]*TAPIR 350-17, California Institute of Technology, 1200 E California Boulevard, Pasadena, California 91125, USA*
[2]*Max Planck Institute for Gravitational Physics (Albert Einstein Institute), D-14476 Potsdam, Germany*
[3]*Department of Physics, Cornell University, Ithaca, New York 14853, USA*
[4]*Cornell Center for Astrophysics and Planetary Science, Cornell University, Ithaca, New York 14853, USA*
[5]*Department of Mathematics, Center for Scientific Computing and Data Science Research, University of Massachusetts, Dartmouth, Massachusetts 02747, USA*
[6]*Department of Physics and Astronomy, The University of Mississippi, University, Mississippi 38677, USA*
[7]*Department of Physics and Astronomy, University of New Hampshire, 9 Library Way, Durham, New Hampshire 03824, USA*
[8]*Department of Physics and Astronomy, Washington State University, Pullman, Washington 99164, USA*

(Received 23 April 2023; accepted 2 June 2023; published 28 June 2023)

We present a numerical-relativity simulation of a black hole-neutron star merger in scalar-tensor (ST) gravity with binary parameters consistent with the gravitational wave event GW200115. In this exploratory simulation, we consider the Damour-Esposito-Farèse extension to Brans-Dicke theory, and maximize the effect of spontaneous scalarization by choosing a soft equation of state and ST theory parameters at the edge of known constraints. We extrapolate the gravitational waves, including tensor and scalar (breathing) modes, to future null-infinity. The numerical waveforms undergo ∼22 wave cycles before the merger, and are in good agreement with predictions from post-Newtonian theory during the inspiral. We find the ST system evolves faster than its general-relativity (GR) counterpart due to dipole radiation, merging a full gravitational-wave cycle before the GR counterpart. This enables easy differentiation between the ST waveforms and GR in the context of parameter estimation. However, we find that dipole radiation's effect may be partially degenerate with the NS tidal deformability during the late inspiral stage, and a full Bayesian analysis is necessary to fully understand the degeneracies between ST and binary parameters in GR.

DOI: 10.1103/PhysRevD.107.124051

I. INTRODUCTION

Increasing numbers of gravitational-wave (GW) events [1–4] have allowed us to probe the extreme gravity environment near the coalescence of a compact binary system, which opens up a new chapter for tests of general relativity (GR) [1,5–25]. To robustly test GR, there is a need for accurate GW predictions both in GR and beyond-GR theories, so that one can use Bayesian model selection to ascertain which theory better agrees with GW observations.

Scalar-tensor (ST) theory [26–29] is the simplest alternative theory of gravity, where the strength of gravity is modulated by scalar field(s). The original formulation of ST theory was due to Jordan [26], Fierz [27], Brans and Dicke [28,29] (JFBD), and was generalized by Bergmann [30] and Wagoner [31] to capture more general conformal factors, and by Damour and Esposito-Farèse [32] to multiple scalar fields. An important feature of ST theory is scalar radiation, an extra energy dissipation channel in addition to the usual tensor radiation in GR. The leading scalar radiation is dipolar, and thus more important at low frequencies than the quadrupolar waves that control a GR inspiral [13,32–46]. Under this effect, the evolution of some strong-gravity systems can deviate from the prediction of GR and leave imprints on observables. For instance, binary-pulsar systems have been shown to be a good laboratory [33,34,39,47–59] (see also Refs. [6,60–66] for reviews) since the celebrated Hulse-Taylor PSR B1913 + 16 [67]. By measuring the orbital decay rate of the systems, one can examine and constrain ST theory via the parametrized post-Keplerian formalism [47,48,66,68].

The strength of the dipole radiation depends on the scalar charge $\alpha_{\rm NS}$ [32,57,69,70], which characterizes the ability of an object to condense the scalar field. The scalar charge of a

*sma@caltech.edu
†vijay.varma@aei.mpg.de

black hole (BH) vanishes as the no-hair theorems have been shown to apply in ST [23,71–74]. For a binary system, the dipole radiation power is proportional to its charge difference squared [33]: $(\alpha_A - \alpha_B)^2$, where A and B refer to the two objects in the binary system. Consequently, if two objects possess similar scalar charges, such as in near equal-mass binary neutron star (BNS) systems where both stars are similarly scalarized, the dipole radiation is suppressed. Conversely, the best tests of ST can come from a mixed system that consists of a neutron star (NS) and a BH, as only one of them carries scalar charge.

While ST theory is strongly constrained in some environments, deviations from GR could also be amplified if a NS undergoes *spontaneous scalarization*[1] in certain conditions [75–84], as pointed out by Damour and Esposito-Farèse [48,69]. At some critical central density, the equilibrium solutions for NSs' structures bifurcate into several branches, and the GR branch becomes unstable [85,86]. The most stable solution corresponds to a scalarized NS with a much larger scalar charge [32,57,69,70]. Therefore, the dipole radiation and consequential deviations from GR are significantly amplified in such scalarized BHNS systems, which makes them, if they exist, ideal environments for studying ST theory.

The LIGO-Virgo detectors [87,88] recently made the landmark observations of the first BHNS binaries via GWs, GW200105 and GW200115 [89]. With the upcoming improvement in GW detector sensitivity [90], including future third-generation detectors [91–94], we can look for effects of gravitational dipole radiation at ever-increasing precision. Therefore, it is timely and vital to give a precise prediction of the evolution of the scalarized BHNS binaries in ST, especially accurate modeling of their dipole GW waveforms. Although there have been significant post-Newtonian (PN) efforts dedicated toward constructing waveforms in ST theory[2] [13,32–46,97], PN theory breaks down as one approaches the merger, or for strongly scalarized NSs. To date, numerical relativity (NR) still remains the only *ab initio* method to investigate ST theory near the merger [74–76,98–104]. For compact binaries, NR has been used to simulate binary black holes (BBHs) [74] and BNSs [75,76,104] in ST. A numerical simulation of a scalarized BHNS system is still missing. In this work, we aim to fill this gap by performing fully nonlinear NR simulations of a BHNS merger in ST theory, with a particular focus on how GW emission is impacted by spontaneous scalarization. Motivated by the LIGO-Virgo observations, we consider a GW200115-like system [89].

This paper is organized as follows. In Sec. II we give a brief introduction to ST theory and our simulation algorithm. Section III concentrates on our numerical setup and strategy to maximize the effect of spontaneous scalarization. Section IV provides our major simulation results. Next in Sec. V we investigate distinguishability between waveforms in GR and ST, with a particular focus on to what extent the ST waveform can be mimicked by tidal effects predicted by GR. Finally in Sec. VI we provide some concluding remarks.

Throughout this paper we use the geometric units with $c = G_* = 1$, where G_* is the bare gravitational constant in the Jordan frame. We use the total Jordan-frame mass to normalize all dimensional quantities (e.g., time and distance). Meanwhile, we use the Latin letters $a, b, c\ldots$ for spacetime indices, and $i, j, k\ldots$ to represent spatial indices.

II. EQUATIONS OF MOTION AND NUMERICAL METHODS

In this work we consider a ST theory with a single massless scalar field ϕ. We first provide some basic features and equations of motion of this theory in Sec. II A. Then in Sec. II B we introduce our numerical algorithm to perform the NR simulation. Finally in Sec. II C we provide our method for extrapolating the waveform to future null infinity.

A. The Jordan and Einstein frames

The ST theory is governed by the action [30,31]

$$S = \int d^4x \frac{\sqrt{-g}}{16\pi}\left[\phi R - \frac{\omega(\phi)}{\phi}\nabla_c\phi\nabla^c\phi\right] + S_M[g_{ab}, \Psi_m], \tag{1}$$

where g_{ab} is the metric, g is the metric determinant, R is the Ricci scalar, S_M is the action for all matter fields Ψ_m, and $\omega(\phi)$ is an arbitrary function of ϕ that parameterizes the coupling between the scalar field and metric. The action in Eq. (1) is written in the *Jordan frame* in which ϕ is nonminimally coupled with the metric g_{ab}, whereas the matter fields are minimally coupled to the metric and not coupled with the scalar field ϕ, as required by the weak equivalence principle. Therefore, test particles follow the geodesics of the Jordan frame metric. NSs are treated as perfect fluids and are governed by the law of conservation of baryon number and energy momentum:

$$\nabla_a(\rho_0 u^a) = 0, \tag{2a}$$

$$\nabla_a T^{ab} = 0, \tag{2b}$$

where T^{ab} is the stress-energy tensor in the Jordan frame. The stress-energy tensor for an perfect fluid reads

$$T_{ab} = \rho_0 h u_a u_b + P g_{ab}, \tag{3}$$

[1]See Refs. [75–80] for two related phenomena: induced and dynamical scalarization.

[2]See also Refs. [95,96] for an effective-field-theory approach.

with ρ_0 the rest mass density of the fluid, h the specific enthalpy, P the pressure, and u_a the 4-velocity.

The equations of motion for the metric and the scalar field take complicated forms in the Jordan frame [see Eq. (2.6) of Ref. [9] for example]. In particular, the principal symbols of the PDE system is not diagonal in the (g_{ab}, ϕ) field space, so it is not manifestly symmetric-hyperbolic.[3] Consequently, the Jordan frame sometimes is not ideally suited for simulating the metric and scalar fields. A standard approach to get around this issue is to apply a conformal transformation [32]: $\bar{g}_{ab} = \phi g_{ab}$. Then the action becomes:

$$S = \int d^4x\sqrt{-\bar{g}}\left[\frac{\bar{R}}{16\pi} - \frac{1}{2}\nabla_c\psi\nabla^c\psi\right] + S_M\left[\frac{\bar{g}_{ab}}{\phi}, \Psi_m\right], \tag{4}$$

where $\bar{R}$ is the Ricci scalar derived from $\bar{g}_{ab}$, and

$$d\psi = \sqrt{\frac{3+2\omega}{16\pi}}\frac{d\phi}{\phi}. \tag{5}$$

The integration of Eq. (5) depends on the form of $\omega(\phi)$, and we will explain more details below in Eqs. (17) and (18). The transformed metric $\bar{g}_{ab}$ defines a new frame, called the *Einstein frame*; and the scalar field ψ is minimally coupled in the gravitational sector. The corresponding equations of motion become manifestly symmetric-hyperbolic:

$$\bar{G}_{ab} = 8\pi(\bar{T}^{\psi}_{ab} + \bar{T}_{ab}), \tag{6a}$$

$$\bar{\Box}\psi = \frac{1}{2}\frac{d\log\phi}{d\psi}\bar{T}. \tag{6b}$$

Note that the principal part of the gravitational sector is now identical to its GR counterpart. Here $\bar{G}_{ab}$ is the Einstein tensor obtained from $\bar{g}_{ab}$, $\bar{T}_{ab} = T_{ab}/\phi$ is the matter stress-energy tensor in the Einstein frame, $\bar{T} = \bar{g}^{ab}\bar{T}_{ab}$ is its trace, and $\bar{T}^{\psi}_{ab}$ is the stress-energy tensor of the scalar field, given by

$$\bar{T}^{\psi}_{ab} = \nabla_a\psi\nabla_b\psi - \frac{1}{2}\bar{g}_{ab}\nabla_c\psi\nabla^c\psi. \tag{7}$$

On the other hand, a complication of the Einstein frame is that the hydrodynamic equations gain additional source terms:

$$\bar{\nabla}_a\bar{T}^{ab} = -\frac{1}{2}\frac{d\log\phi}{d\psi}\bar{T}\nabla^b\psi, \tag{8a}$$

$$\bar{\nabla}_a(\bar{\rho}_0\bar{u}^a) = -\frac{1}{2}\frac{d\log\phi}{d\psi}\bar{\rho}_0\bar{u}^a\nabla_a\psi. \tag{8b}$$

[3]Nevertheless, well-posed formulations of ST theories have been found by Salgado *et al.* [105,106].

The scalar field ψ is now directly coupled with the matter fields. Because of the source terms on the right-hand side (rhs), particles do not follow geodesics of $\bar{g}_{ab}$.

B. Numerical algorithm

The single-scalar-field ST theory has been solved numerically for BBHs [74] and BNSs [75,76], with the pure Einstein frame [74,75], and the pure Jordan frame [76]. In our case, we simulate the BHNS system using the spectral Einstein code (SpEC) [107], developed by the Simulating eXtreme Spacetimes (SXS) collaboration [108]. SpEC adopts the generalized harmonic formalism [109], where the Einstein equations are cast into a first-order symmetric hyperbolic (FOSH) form. It is ideal to use SpEC to evolve the metric and the scalar field sectors in the Einstein frame [Eq. (6)]. The reason is twofold. (a) The equations of motion in the Einstein frame are manifestly symmetric-hyperbolic, as mentioned in Sec. II A. Therefore the well-posedness of the Cauchy problem is straightforwardly established. (b) The principal parts of Eq. (6) are identical to that of GR with a Klein-Gordon field. Consequently, we can utilize the existing GR FOSH system [109] and the FOSH system for scalar fields [110,111] to perform the simulations.

For the hydrodynamics, one could in principle approach the problem in the same Einstein frame by evolving Eq. (8). But this will complicate the problem because the extra source terms in Eq. (8), which depend on the scalar field, need to be added to the existing hydrodynamic code infrastructure in SpEC [112]. Furthermore, any routine in SpEC that assumes the simple form of energy-momentum and Baryon number conservation in Eq. (2) will need to be revisited. To save the amount of code changes required, here we propose a simpler algorithm to fulfill the goal.

We adopt a hybrid scheme, illustrated in Fig. 1. We evolve the hydrodynamic system in the Jordan frame, where the corresponding equations [Eq. (2)] are the same as their GR counterparts due to the weak equivalence principle. This lets us use the entire relativistic hydrodynamics module without modification. Meanwhile, we use the FOSH systems to treat the metric and the scalar field in the Einstein frame. Since the Jordan and Einstein frames are related, a proper data flow needs to be established to evolve them together. An essential step is to pass the Jordan-frame metric g_{ab} and stress-energy tensor T_{ab} back and forth (see Appendix A for details): The Einstein-frame metric $\bar{g}_{ab}$ is converted to its Jordan-frame version g_{ab} via $g_{ab} = \bar{g}_{ab}/\phi$, then g_{ab} is sent to the Jordan frame for evolving the hydrodynamics. Similarly, the Jordan-frame stress-energy tensor T_{ab} is converted to the Einstein-frame one through $\bar{T}_{ab} = T_{ab}/\phi$, and inserted into the Einstein equations in Eq. (6).

Within SpEC, this communication is made easier by the two-grid method already used in hydrodynamics simulations [112], wherein the metric sector is evolved on a pseudospectral grid, while the hydrodynamic equations are

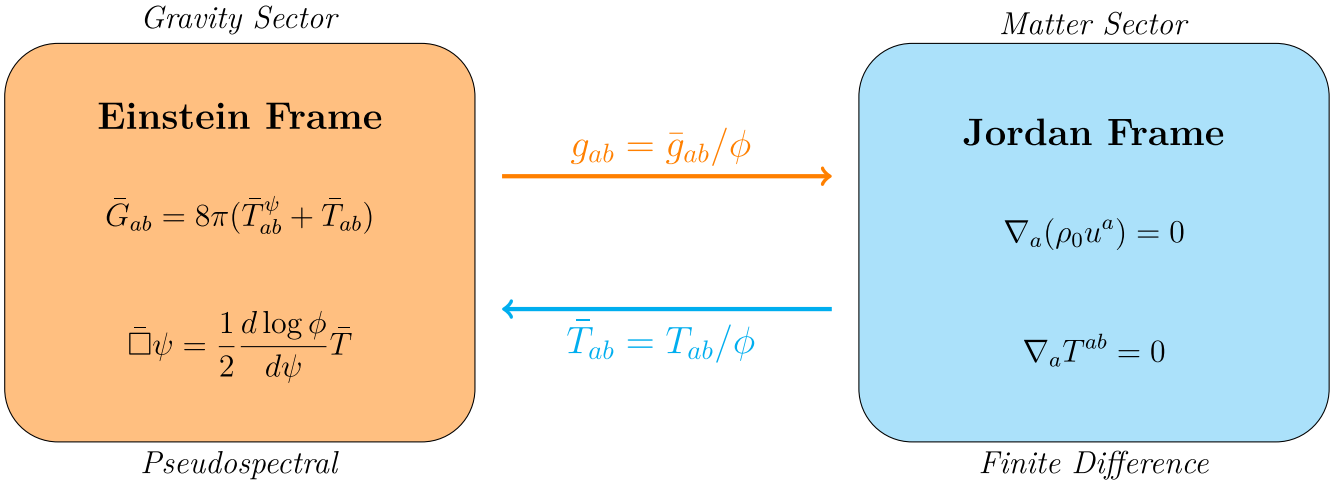

FIG. 1. The algorithm of our numerical simulations. We use pseudospectral methods to evolve the Einstein-frame metric and scalar field, while we use shock-capturing finite difference to simulate the Jordan-frame matter fields. In practice, we convert the Einstein-frame metric $\bar{g}_{ab}$ to the Jordan-frame one via $g_{ab} = \bar{g}_{ab}/\phi$, and then send g_{ab} to the finite difference domain for hydrodynamics simulations. Similarly, we transfer the Jordan-frame stress-energy tensor T_{ab} from the finite difference grid to the pseudospectral grid, convert it to the Einstein-frame stress-energy tensor through $\bar{T}_{ab} = T_{ab}/\phi$, and then insert $\bar{T}_{ab}$ into the Einstein equations in Eq. (6).

evolved on a finite difference grid that can handle shocks. At each time step, the metric from the pseudospectral grid is already interpolated onto the finite difference grid and is fed to the hydrodynamic equations, and the matter fields are passed by interpolation from the finite difference grid to the pseudospectral grid and are fed to the stress-energy tensor in the Einstein equations. For the ST simulations, the metric and the scalar field are evolved in the Einstein frame [see Eq. (6)] on the pseudospectral grid, but before the metric is interpolated to the finite difference grid, it is first converted to the Jordan frame. Similarly, the hydrodynamics equations [see Eq. (2)] are evolved in the Jordan frame, but before the matter terms are transformed to the Einstein frame, they are first interpolated to the pseudospectral grid.

C. Waveform extrapolation

One of the most important tasks of our numerical simulations is to compute GWs at future null infinity, where we approximate GW detectors to reside. Methods have been developed, including wave extrapolation [113,114] and Cauchy-characteristic extraction (CCE) [115,116], to extract the GWs from simulations with finite domains. This paper adopts the extrapolation method and leaves CCE for future work.

Following the standard treatment in PN theory [36,42,43,45], we define a new conformally transformed metric $\tilde{g}_{ab}$ by

$$\tilde{g}_{ab} = (\phi/\phi_0)g_{ab} = \bar{g}_{ab}/\phi_0, \tag{9}$$

which differs from the Einstein frame metric $\bar{g}_{ab}$ by a factor of ϕ_0, the asymptotic value of the scalar field. The factor is introduced so that the metric $\tilde{g}_{ab}$ takes its Minkowski form $\eta_{ab} \equiv \mathrm{diag}(-1,1,1,1)$ far from the system. In our simulations, we find that the value of ϕ_0 is always close to 1, and the difference is negligible, so we will not distinguish $\tilde{g}_{ab}$ from $\bar{g}_{ab}$ below. The gravitational perturbation $\tilde{h}_{ab}$ associated with $\tilde{g}_{ab}$ is given by

$$\tilde{h}^{ab} = \eta^{ab} - \sqrt{-\tilde{g}}\tilde{g}^{ab}, \tag{10}$$

whose indices are raised and lowered by η^{ab}. Then the Jordan-frame metric can be written as [42]

$$g_{ab} = \eta_{ab} + \tilde{h}_{ab} - \frac{1}{2}\tilde{h}\eta_{ab} - \Psi\eta_{ab} + \mathcal{O}\left(\frac{1}{r^2}\right), \tag{11}$$

where

$$\Psi = \frac{\phi - \phi_0}{\phi_0}. \tag{12}$$

Due to the equation of geodesic deviation [117], the GW measured by a detector corresponds to the components of the Riemann curvature tensor,

$$R_{0i0j} = -\frac{1}{2}\ddot{\tilde{h}}^{\mathrm{TT}}_{ij} - \frac{1}{2}\ddot{\Psi}(\hat{N}_i\hat{N}_j - \delta_{ij}), \tag{13}$$

where "TT" refers to the transverse-traceless projection of $\tilde{h}_{ij}$, and $\hat{N}_i$ is GW's propagation direction. As a result, the tensor field $\tilde{h}^{\mathrm{TT}}_{ij}$ contributes to the $+$ and $\times$ polarizations of the GW signal as in GR, while the scalar field Ψ corresponds to a transverse breathing mode.[4]

[4]Longitudinal and vector polarizations vanish in ST gravity [117].

TABLE I. Summary of the parameters of the GW200115-like BHNS system we consider. The NS has a baryonic mass $m^{\rm B}$ and a Jordan-frame mass $m^{\rm J}_{\rm NS}$. Its radius in the Jordan frame is $R^{\rm J}_{\rm ST}$. In the absence of the scalar field, its radius is $R_{\rm GR}$, and $C_{\rm GR} = m^{\rm J}_{\rm NS}/R_{\rm GR}$ is its compactness. The GR tidal Love number of the NS is $k_2^{\rm GR}$; $\Lambda_2^{\rm GR}$ is the corresponding tidal deformability; $\alpha_{\rm NS}$ is its scalar charge. To maximize the effect of spontaneous scalarization, we choose $(\beta_0, \alpha_0) = (-4.5, -3.5 \times 10^{-3})$. The BH has a Jordan-frame mass $m^{\rm J}_{\rm BH}$. Its dimensionless spin along is denoted by $\boldsymbol{\chi}^{\rm BH}_{\rm init}$ and is antialigned with the Newtonian angular momentum direction $\hat{\boldsymbol{L}}_N$. The mass-weighted tidal deformability of the BNHS system is $\tilde{\Lambda}_2^{\rm GR}$. $R_{\rm bdry}$ indicates the radius of the simulation domain, in the unit of total mass $M = 7.2M_\odot$, and $N_{\rm cycle}$ is the number of orbital cycles before merger. The remnant is a BH with mass m_f and spin χ_f, where m_f is in the unit of M.

$m^{\rm B}/M_\odot$	$m^{\rm J}_{\rm NS}/M_\odot$	$\chi^{\rm NS}_{\rm init}$	$R^{\rm J}_{\rm ST}$/km	$R_{\rm GR}$/km	$C_{\rm GR}$	$k_2^{\rm GR}$	$\Lambda_2^{\rm GR}$
1.71	1.5	0.0	10.58	10.55	0.21	0.0803	131.1

$\alpha_{\rm NS}$	$m^{\rm J}_{\rm BH}/M_\odot$	$\boldsymbol{\chi}^{\rm BH}_{\rm init}$	$\tilde{\Lambda}_2^{\rm GR}$	$R_{\rm bdry}/M$	$N_{\rm cycle}$	m_f/M	χ_f
0.18	5.7	$-0.19\hat{\boldsymbol{L}}_N$	2.95	500	12	0.98	0.38

To extract the three GW polarizations from our numerical simulations, we notice that the gravitational perturbation $\tilde{h}_{ab}$ is associated with the Einstein-frame metric $\bar{g}_{ab}$, so we can restrict ourselves to this frame during the extrapolation. On the scalar sector side, ψ [defined in Eq. (5)] is our evolved variable in the Einstein frame. We can convert it to the observable Ψ by integrating Eq. (5) and then inserting the result into Eq. (12). Note that the integration depends on the form of $\omega(\phi)$ and we will provide more details in Eq. (17). In practice, we first measure the values of $\tilde{h}$ and ψ at multiple extraction radii at each timestep, and then extrapolate their values to null infinity $\mathcal{I}^+$. For each radius, we decompose $\tilde{h} = \tilde{h}_+ - i\tilde{h}_\times$ and ψ into a sum over a set of (spin-weighted) spherical harmonics ${}_sY_{lm}(\iota, \varphi)$,

$$r\tilde{h}/M = \sum_{l,m} {}_{-2}Y_{lm}(\iota, \varphi)\tilde{h}_{lm} + \mathcal{O}(r^{-1}), \tag{14a}$$

$$r\psi/M = \sum_{l,m} Y_{lm}(\iota, \varphi)\psi_{lm} + \mathcal{O}(r^{-1}), \tag{14b}$$

where we used the fact that $\tilde{h}, \psi \sim 1/r$ in the wave zone. Each field $\tilde{h}_{lm}$ and ψ_{lm} is extrapolated to $\mathcal{I}^+$ following the algorithm outlined in Refs. [114,118–120], with the Python package SCRI [121,122]. In particular, the null rays are parametrized by an approximate retarded time u, given by

$$u = t_{\rm corr} - r_*, \tag{15}$$

with

$$r_* = r + 2M^{\rm E} \log\left(\frac{r}{2M^{\rm E}} - 1\right), \tag{16}$$

where $M^{\rm E} = m^{\rm E}_{\rm NS} + m^{\rm E}_{\rm BH}$ is the total Einstein-frame mass, and we refer to Refs. [113,114] for the expression of the corrected time $t_{\rm corr}$. Finally these fields are interpolated to common sets of u and fit in powers of $1/r$, allowing to approximate the $r \to \infty$ limit.

III. BINARY AND SCALAR PARAMETERS

In Sec. III A, we provide the binary parameters we consider for the BHNS system, which are chosen to be consistent with GW200115 [89]. Then in Sec. III B, we introduce our strategy for choosing the parameters of the scalar field and the NS. As mentioned in Introduction, a NS can undergo significant scalarization under certain conditions, leading to non-negligible dipole radiation while the scalarized NS orbits in the binary system. This extra energy dissipation channel accelerates the evolution of the BHNS system and thus makes the emitted GWs distinguishable from their GR counterparts. In our simulations, we want to highlight such distinctions by optimally picking the ST theory parameters and the EOS of the NS.

A. The binary parameters

We summarize the parameters of the GW200115-like BHNS system [89] we consider in Table I. The binary system consists of a nonrotating NS with a Jordan-frame mass $m^{\rm J}_{\rm NS}$ of $1.5M_\odot$, and a spinning BH with $m^{\rm J}_{\rm BH} = 5.7M_\odot$. The dimensionless spin of the BH $\chi^{\rm BH}_{\rm init}$ is -0.19, i.e., it is antialigned with the orbital angular momentum. We set the initial separation between the BH and the NS $D_{\rm init}$ to $11.7M$, where $M \equiv m^{\rm J}_{\rm BH} + m^{\rm J}_{\rm NS} = 7.2M_\odot$ is the total Jordan-frame mass; and place the outer boundary of the system at $R_{\rm bdry} = 500M$. The system undergoes $N_{\rm cycle} \sim 12$ cycles prior to the merger. The orbital eccentricity is reduced iteratively to $e_{\rm orb} \sim 1.6 \times 10^{-4}$ [123].

Due to our two-grid method described in Fig. 1, the NS resides in the Jordan frame while the BH is in the Einstein frame. So in practice one needs to specify the Einstein-frame mass of the BH $m^{\rm E}_{\rm BH}$ instead, which is related to the Jordan-frame mass $m^{\rm J}_{\rm BH}$ through [32]

$$m_{\rm BH}^{\rm E} = \frac{m_{\rm BH}^{\rm J}}{\sqrt{\phi}},$$

where ϕ is evaluated at the position of the BH. We find that $|\phi - 1| \lesssim 5 \times 10^{-5}$ in the vicinity of the BH, during the inspiral stage, therefore the difference between $m_{\rm BH}^{\rm J}$ and $m_{\rm BH}^{\rm E}$ is negligible; thus we simply set $m_{\rm BH}^{\rm E} = 5.7 M_\odot$.

B. The parameters of the scalar field and the NS

For a given Jordan-frame mass $m_{\rm NS}^{\rm J}$, the strength of spontaneous scalarization for the NS depends on $\omega(\phi)$, as well as the EOS and compactness [70,124]. To look for the optimal choices to maximize the scalarization in our BHNS simulation, we consider a single Tolman-Oppenheimer-Volkoff (TOV) NS in an isolated gravity environment and investigate the impact of the scalar field on the stellar internal structure.

The function $\omega(\phi)$ characterizes the coupling between the scalar field and gravity. In this work we follow Ref. [125], whose idea was to Taylor expand the coupling function $\ln\phi$ in ψ,

$$\phi = \exp\left[-4\sqrt{\pi}\alpha_0(\psi - \psi_0) - 4\pi\beta_0(\psi - \psi_0)^2\right]. \quad (17)$$

Using Eq. (5), we obtain

$$\omega = \frac{1}{2}\frac{1}{[\alpha_0 + \sqrt{4\pi}\beta_0(\psi - \psi_0)]^2} - \frac{3}{2}. \quad (18)$$

Here ψ_0 is the asymptotic value of ψ that can also be associated with cosmological expansion [126–128]. For simplicity, we follow Ref. [75] and set $\psi_0 = 0$. The other two constants α_0 and β_0 determine the features of the ST theory. In particular, if $\beta_0 = 0$ we get the JFBD theory [26–29], which is parametrized by $\alpha_0 = -(3 + 2\omega_{\rm BD})^{-1/2}$, where $\omega_{\rm BD}$ is the Brans-Dicke (BD) parameter. In the low-density solar system environment, its value is severely restricted to $\omega_{\rm BD} > 40000$ by the Cassini mission [6,129], which corresponds to $|\alpha_0| \lesssim 3.5 \times 10^{-3}$. In addition, current binary pulsar measurements place a constraint $\beta_0 \gtrsim -4.5$, because no spontaneous scalarization has been detected yet [9]. See also Refs. [53–55,58] for more recent updates.

As pointed out by Damour and Esposito-Farèse [48,125], even though a scalar-tensor theory with $|\alpha_0| \ll 1$ is indistinguishable from GR within the weak-gravity regime, a negative value of β_0 can lead to significant relativistic deviations in a strong-gravity environment, such as spontaneous scalarization of a NS. The size of the scalarization is characterized by the scalar charge $\alpha_{\rm NS}$ [32,125]. In this paper, we adopt the definition of $\alpha_{\rm NS}$ from Refs. [32,125], which differs from the convention used by the PN community by a minus sign (see Appendix A of Ref. [43] for translating notation); consequently, we have $\alpha_{\rm NS} < 0$. For a Newtonian star, $\alpha_{\rm NS}$ reduces to α_0; thus is independent of its internal structure (a proof can be found in Appendix B). For a strongly self-gravitating scalarized star, its structure is governed by the TOV equation with an extra scalar field, see, e.g., Eqs. (7)–(9) of Ref. [125]; we provide a brief review in Appendix B. We numerically solve the TOV equation, and the choice of the EOS will be discussed shortly. Then we compute the corresponding scalar charge $\alpha_{\rm NS}$ with Eq. (B5). Figure 2 shows $\alpha_{\rm NS}$ as a function of the Jordan-frame mass $m_{\rm NS}^{\rm J}$, using a variety of β_0 (the upper panel, with α_0 being fixed to -3.5×10^{-3}) and α_0 (the lower panel, with β_0 being fixed to -4.5) values. Notice that sharp transitions develops at $m_{\rm NS}^{\rm J} \sim 1.4 M_\odot$ and $1.8 M_\odot$ as $\alpha_0 \to 0$. The NSs between these masses are spontaneously scalarized. In addition, we see the scalar charge increases with the absolute value of α_0

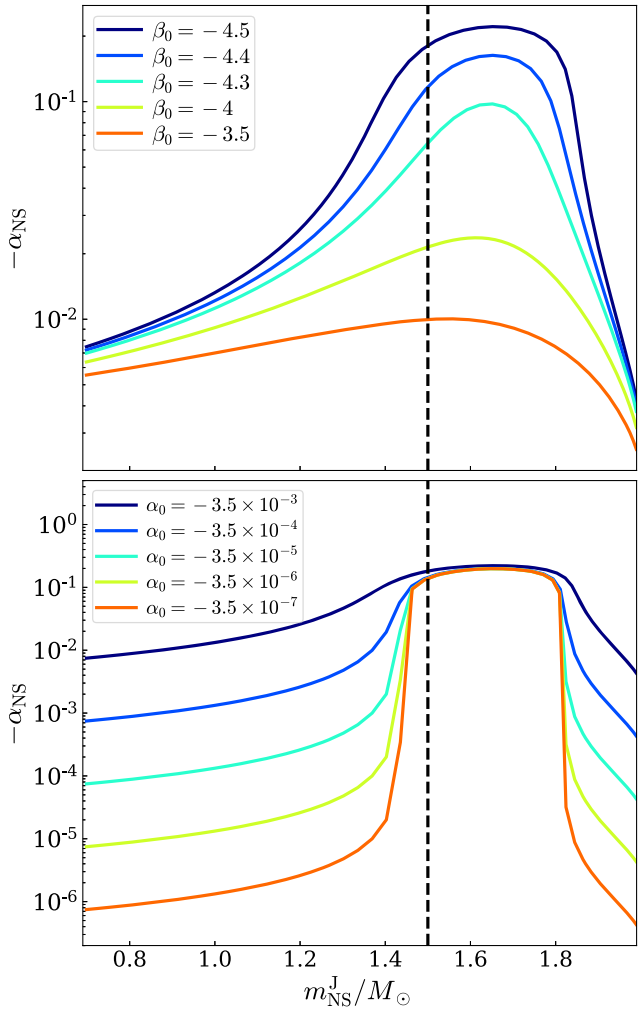

FIG. 2. The scalar charge of a NS as a function of $m_{\rm NS}^{\rm J}$, with a variety of α_0, β_0. Upper panel: varying β_0 while $\alpha_0 = -3.5 \times 10^{-3}$; lower panel: varying α_0 with $\beta_0 = -4.5$. The EOS is summarized in Table I, which has been selected to amplify the scalarization. The vertical dashed lines correspond to the NS in our simulation ($m_{\rm NS}^{\rm J} = 1.5 M_\odot$). We choose $\psi_0 = 0$ in both panels.

and β_0 for a fixed $m_{\rm NS}^{\rm I}$ (e.g. the vertical dashed line). Therefore, we chose $(\beta_0, \alpha_0) = (-4.5, -3.5 \times 10^{-3})$ below to maximize the effect of scalarization.

On the other hand, we can also leverage the freedom of choosing an EOS to magnify the scalarization. Here we restrict ourselves to the spectral EOSs provided in [130], which allows a broad range of cold and beta-equilibrium EOSs (see Fig. 1 of Ref. [130]). The parametrization reads

$$P(\rho) = \begin{cases} \kappa_0 \rho^{\Gamma_0}, & \rho < \rho_0, \\ P_0 \exp\left[\int_0^x \Gamma(\tilde{x}) d\tilde{x}\right], & \rho > \rho_0, \end{cases} \tag{19}$$

with ρ_0 a reference density, $P_0 = P(\rho_0)$, $\Gamma(x) = \gamma_2 x^2 + \gamma_3 x^3$ and $x = \ln(\rho/\rho_0)$. Among the options, we find the following soft EOS that gives rise to the strongest scalarization effect (obtained from Table III of Ref. [130]):

$$\Gamma_0 = 2, \quad \rho_0 = 8.44019 \times 10^{-5}, \quad P_0 = 1.20112 \times 10^{-7}$$
$$\gamma_2 = 0.475296, \quad \gamma_3 = -0.117048.$$

Note that ρ_0 and P_0 are in $G_* = c = M_\odot = 1$ units. This specific EOS can produce macroscopic properties that are compatible with current constraints, including the mass-radius relation, tidal deformability, and maximum NS mass [130]. However, it should be noted that this EOS lacks composition and temperature dependence [130], which makes it less realistic in those aspects.

For comparison, we also solve a NS with the same Jordan-frame mass in GR, and summarize the corresponding stellar properties in Table I. The compactness of the NS is $C_{\rm GR} \sim 0.22$, with a tidal Love number $k_2^{\rm GR}$ of ∼0.08 [131] and a tidal deformability $\Lambda_2^{\rm GR} = \frac{2}{3}\frac{k_2^{\rm GR}}{C_{\rm GR}^5}$ of ∼131.1 [132] in the absence of the scalar field.

To end this section, we emphasize that our choices for the EOS and the ST theory parameters are intentionally made to produce a large scalar field: the values of (α_0, β_0) lie on the edge of existing constraints [6,9,53–55,129], even though they may not be preferred in the actual astrophysical environment. The current idealized configuration is to justify our simulation code and to investigate the maximum possible detectability of the dipole radiation emitted by BHNS systems. Future work is being planned to explore more moderate scenarios.

IV. NUMERICAL RESULTS

We present our main simulation results in this section. For comparison, the BHNS system is evolved in both GR and ST theory, and two numerical resolutions are adopted for each case by specifying different numerical error tolerances to the adaptive mesh refinement (AMR) algorithm in SpEC [133]. Below we first give a qualitative panorama view of the GR system in Sec. IV A, and the ST system in Sec. IV B. Then in Sec. IV C we compare the GR and ST simulations. Finally in Sec. IV D, we conduct more quantitative discussions by comparing our numerical waveforms to existing PN predictions in ST.

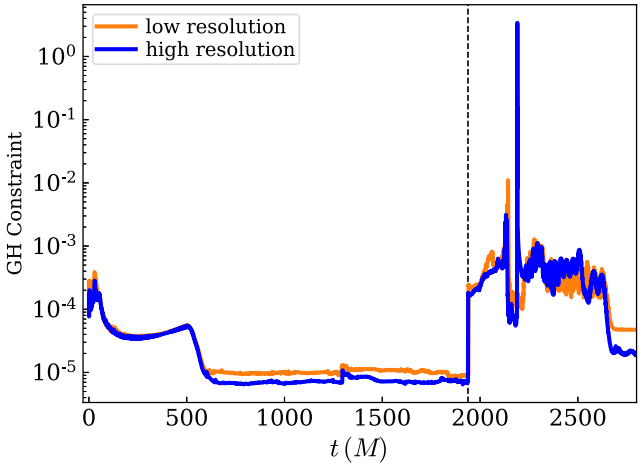

FIG. 3. The evolution of the volume-weighted constraint energy for the metric, evolved with GR. The orange (blue) curve corresponds to the low (high) resolution. The vertical dashed line indicates the onset of the merger.

A. The BHNS system in GR

We first evolve the system with GR, whose initial data are built based on the method in Refs. [134,135]. For the GW200115-like binary parameters we consider (see Table I), the NS is swallowed quickly by the BH during the merger, and there is no tidal disruption. The remnant BH has a mass of $m_f = 0.9785M$, with $M = 7.2M_\odot$ the total Jordan-frame mass defined in Sec. III A. The remnant dimensionless spin is $\chi_f = 0.38$. As a standard numerical diagnostic, we plot the volume-weighted generalized harmonic constraint energy [see Eq. (53) of Ref. [109]] in Fig. 3, where the orange (blue) curve refers to the low (high) resolution run. As expected, the constraint energy decreases with increasing resolution, once the initial transients (known as junk radiation) leave the domain ($t > R_{\rm bdry} = 500M$). Here $R_{\rm bdry}$ is the radius of our simulation domain, as summarized in Table I. In addition, we remark that the constraints jump drastically near $t = 1938M$, when the NS starts to plunge into the BH.

The top panel of Fig. 4 shows the dominant $l = m = 2$ harmonic $\tilde{h}_{22}$ emitted by the BHNS system, with low (in orange) and high (in blue) resolution. We see that the two waveforms manifest significant dephasing near the merger. Our current waveforms are less accurate than other recent BHNS SpEC simulations [136] even though we use the same criteria to set the numerical error tolerances in AMR. This is mainly because the NS we consider is softer, which has a smaller radius and would require finer grids to resolve its structure. However, as the main purpose of this study is to

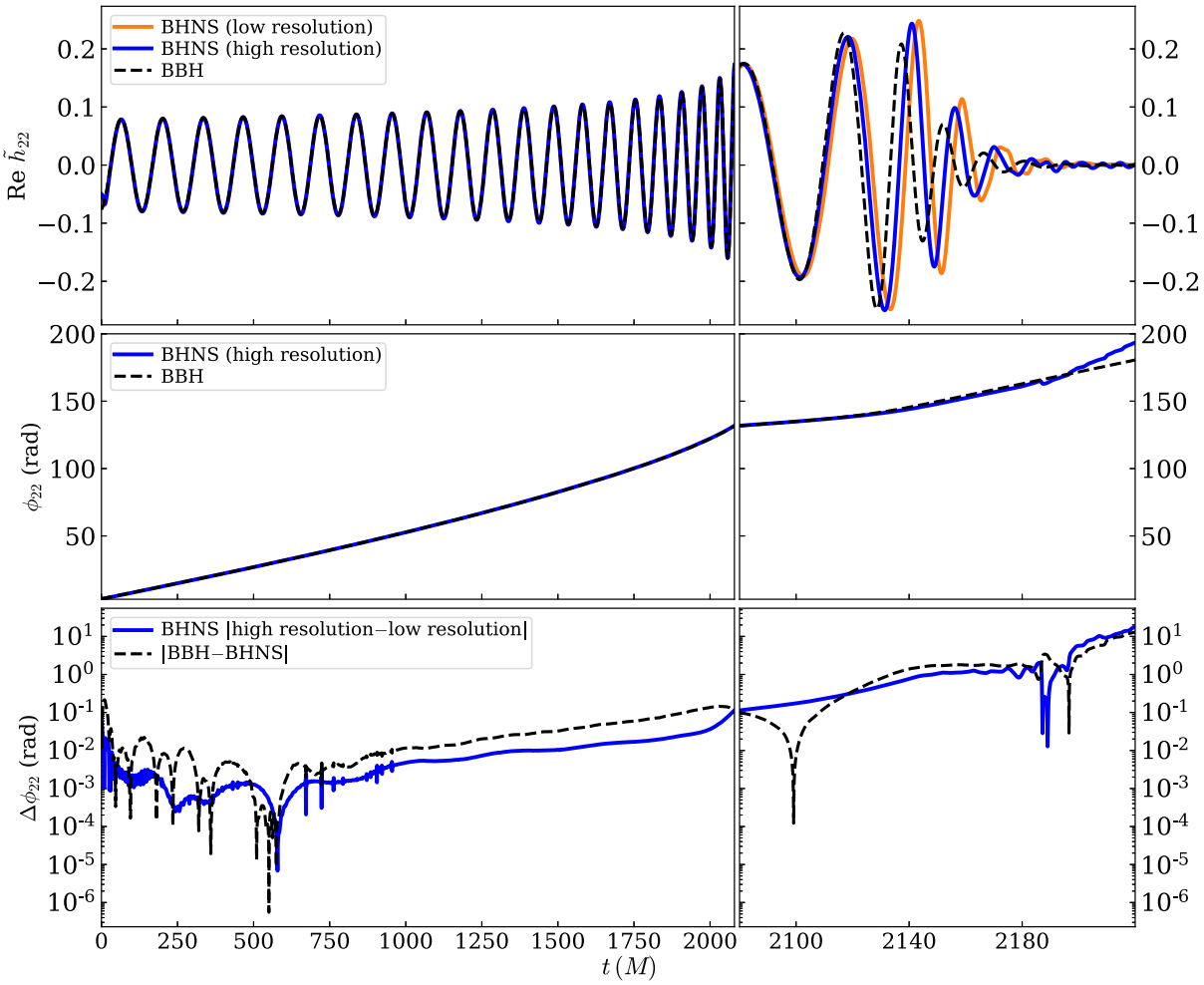

FIG. 4. Upper panels: The GW harmonic $\tilde{h}_{22}$ of the BHNS system evolved with GR, using a low (in orange) and high resolution (in blue). Two BHNS waveforms are compared to that of the BBH system (in black) which has the same mass ratio and spins. We align the three waveforms by minimizing their mismatch over time and phase shifts, with the optimization window chosen to be $[200M, 800M]$. Middle panels: the GW phases of the high-resolution BHNS binary (in blue) and the BBH binary (in black). Lower panels: the GW phase difference between the BBH and the BHNS system (in black). It is compared to the numerical resolution difference of the BHNS waveform (in blue).

get a first qualitative understanding of BHNS binaries in ST, we expect the current accuracy to be sufficient (see more details in Sec. IV C).

The leading tidal effect in the GW phase evolution appears at 5PN order [132], and is captured by a mass-weighted tidal parameter $\tilde{\Lambda}_2^{\rm GR}$ [137]

$$\tilde{\Lambda}_2^{\rm GR} = \frac{16}{13}\frac{(M + 11m_{\rm BH}^{\rm J})}{M^5} m_{\rm NS}^{\rm J\,4}\Lambda_2^{\rm GR}. \tag{20}$$

After plugging in the values listed in Table I, we find $\tilde{\Lambda}_2^{\rm GR}$ is around 2.95, implying that the emitted GWs are almost indistinguishable from that of a BBH system with the same spins and mass ratio. To demonstrate this, we compare the BHNS waveform to that of an equivalent BBH system (black dashed line in the top panel of Fig. 4). The data of the BBH binary are obtained from the `NRSur7dq4` surrogate model [138]. We align the two waveforms $\tilde{h}_{22}^{\rm BHNS}$ and $\tilde{h}_{22}^{\rm Sur}$ by minimizing their mismatch $\mathcal{M}$:

$$\mathcal{M} = 1 - \frac{(\tilde{h}_{22}^{\rm BHNS}|\tilde{h}_{22}^{\rm Sur})}{\sqrt{(\tilde{h}_{22}^{\rm BHNS}|\tilde{h}_{22}^{\rm BHNS})(\tilde{h}_{22}^{\rm Sur}|\tilde{h}_{22}^{\rm Sur})}}, \tag{21}$$

over time and phase shifts. Here the time-domain inner product between two signals a, b is given by

$$(a|b) = \mathrm{Re}\int_{t_1}^{t_2} a(t)^* b(t) dt, \tag{22}$$

where the star denotes complex conjugation, and we choose the optimization window to be $[t_1, t_2] = [200M, 800M]$. We provide the phase evolution ϕ_{22} of the aligned waveforms:

$$\phi_{22} \equiv \arg \tilde{h}_{22}, \tag{23}$$

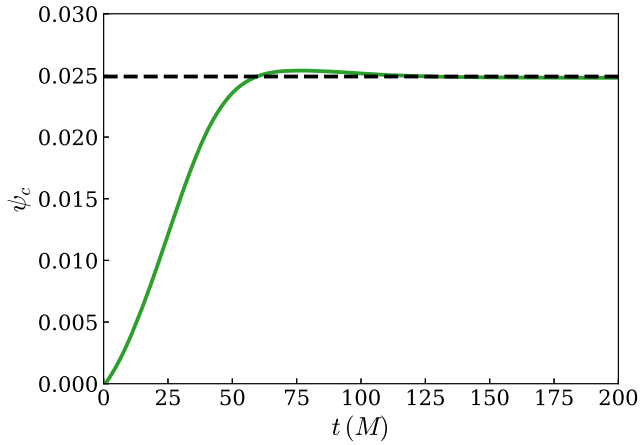

FIG. 5. The evolution of the scalar field ψ measured at the center of the NS. The plot describes the growth of the scalar field around the NS at the beginning of the simulation. The horizontal dashed line corresponds to the prediction by solving equations of motion for an isolated NS in Sec. III B.

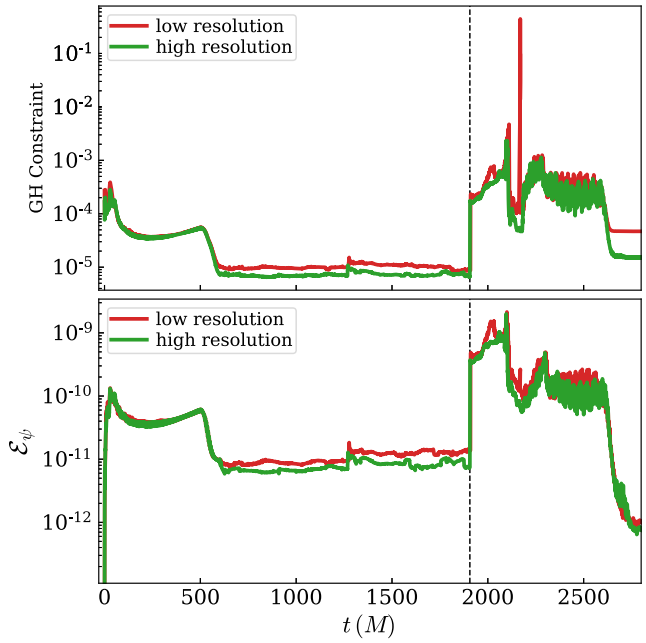

FIG. 6. The evolution of the volume-weighted constraint energy for the metric (the upper panel) and the scalar field (the lower panel), evolved with ST. The red (green) curve corresponds to the low (high) resolution. The vertical dashed line indicates the onset of the merger.

in the middle panel of Fig. 4, as well as the corresponding waveform phase differences $\Delta\phi_{22}$ in the bottom panel. We see the phase difference between the BHNS and BBH ($\sim$0.4 rad) remains comparable to NR numerical resolution difference up to $\sim 10M$ prior to the waveform peak, which indicates that the tidal effect of this system is negligible.

B. The BHNS system in ST: Scalar field

Let us then move on to the ST simulation. For simplicity, we use the same initial data as its GR counterpart to evolve the system, where the scalar field is absent[5]; while this means the initial data do not correctly capture a snapshot of the binary system in ST gravity that started at an infinite time in the past. This is also true for the GR simulation presented in Sec. IV A, where Fig. 3 displays the presence of spurious initial transients during $t < R_{\rm bdry} = 500M$. In our ST simulations, the system undergoes an extra transient regime at the beginning of the evolution, during which a scalar field cloud grows dynamically around the NS. In Fig. 5, we plot the scalar field value ψ_c measured at the stellar center as a function of time. During the first $50M$, the value of ψ_c increases and asymptotes to the value predicted by the isolated NS solver (the horizontal dashed line) that we used in Sec. III B, which serves as a cross-check of our numerical code. Note that the ψ_c growth timescale is much shorter than the aforementioned initial transients ($t \sim 500M$), therefore we expect that our results are not impacted by this additional transition from GR to ST.

We also provide the volume-weighted generalized harmonic constraint energy [see Eq. (53) of Ref. [109]] in the top panel of Fig. 6 and find that the additional scalar field does not worsen the constraint violation compared to the GR system (Fig. 3): the evolution of the constraint is identical modulo a shift to an earlier time, due to the hastened merger of the ST system. In addition, as for the scalar field's FOSH system [110,111], we need to introduce an auxiliary dynamical variable $\Phi_i \equiv \partial_i\psi$, and its associated constraint energy:

$$\mathcal{E}_\psi = \left\| \sqrt{\sum_{i=1}^{3} \left[C_i^{(1)} C_i^{(1)} + C_i^{(2)} C_i^{(2)} \right]} \right\|, \tag{24}$$

where $\|\cdot\|$ denotes L^2 norm over the domain. The derivative constraint for ψ, $C_i^{(1)}$, reads

$$C_i^{(1)} = (\partial_i\psi)_{\rm num} - \Phi_i, \tag{25}$$

where $(\partial_i\psi)_{\rm num}$ corresponds to the numerical spatial derivative of ψ. The second derivative constraint for ψ, $C_i^{(2)}$, is given by

$$C_i^{(2)} = [ijk]\partial_j\Phi_k \qquad (\text{sum on } j,k) \tag{26}$$

with $[ijk]$ being the Levi-Civita symbol, with $[123] = +1$. We provide the evolution of $\mathcal{E}_\psi$ in the lower panel of Fig. 6. As expected, it also decreases with increasing resolution.

Finally, to close this subsection, we give a qualitative description of the scalar field ψ in Fig. 7 by taking a

[5]It is straightforward to check that the GR initial data satisfy the ST constraint equations.

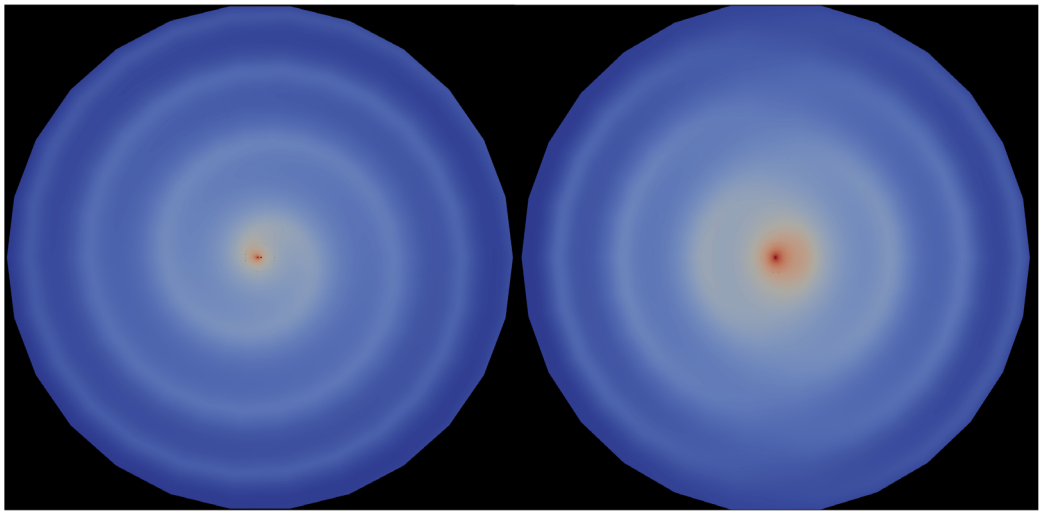

(a) The $x-y$ plane (b) The $y-z$ plane

FIG. 7. A snapshot of the field $\log|\psi|$ at $t = 2062.3M$ across the entire computational domain, with the outer boundary being at $500M$. The orbital angular momentum is aligned with the z axis.

snapshot of its distribution at $t = 2062.3M$ across the entire computational domain. In the wave zone, the distribution of the scalar field in the x–y plane (left panel) is singly periodic in φ like $e^{i\varphi}$, where φ is the azimuthal angle defined in Eq. (14b); and in the y–z plane (right panel), we see vanishing on the z axis with a single maximum at the equatorial plane ($z = 0$), like $\sin\iota$. These patterns are consistent with the dipolar nature $Y_{11} \sim \sin\iota e^{i\varphi}$ of the scalar field, and we will discuss this in more detail in Sec. IV D.

C. Comparison between the GR and ST

Figure 8 displays the evolution of the coordinate separation between the two compact objects for the GR and the ST systems. We first see that the merger portions of both systems can be aligned perfectly through a time shift, namely, they have a similar $\dot{R} - R$ dependence near the merger and thus a similar plunge dynamic, implying a similar orbital separation (and therefore similar frequency) for the onset of the plunge. This feature is different from the BNS simulations in Ref. [75], where ST binaries were found to merge at significantly larger orbital separation (see their Fig. 1). The difference arises from the size of the gravitational attraction. Recall that the gravitational pull in ST gravity is characterized by the effective gravitational constant $G_{\rm eff} = G_*(1 + \alpha_A\alpha_B)$ [32], which is amplified for BNS systems when both the NSs have a nonzero scalar charge. Consequently, their plunges happen at larger orbital separations. By contrast, the gravitational pull in our ST BHNS system is similar to its GR counterpart because the BH's scalar charge vanishes, so the scalar sector has negligible impact on the plunge separation. However, the ST simulation does exhibit a non-negligible deviation from its GR counterpart over a longer timescale. As shown in Fig. 8, the ST simulation has a shorter total duration than the GR case, even though they both start at the same separation. This is because the scalarized NS admits an additional energy dissipation channel via scalar radiation; therefore the system in ST gravity evolves faster during the inspiral.

A direct consequence of the hastened dynamics is a shortening of the GW signal. Figure 9 provides the $l = m = 2$ harmonic of the ST waveform for two different resolutions (solid curves). For reference, $\tilde{h}_{22}$ in GR is plotted as the blue dashed curve. Here we still align the waveforms by minimizing the mismatch in Eq. (21) over time and phase shifts. The same time window $[t_1, t_2] = [200M, 800M]$ is used. After the peak of the ST waveform, it takes the GR waveform an extra GW cycle, $\Delta\phi_{22} \sim 6.34$ rad [Eq. (23)], to reach its peak, smaller than GR's numerical resolution difference at the peak ($\sim$0.6 rad). Therefore our simulations are able to

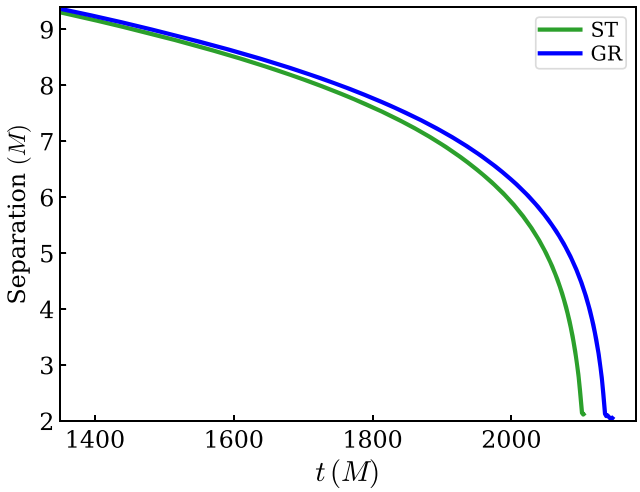

FIG. 8. The evolution of the orbital separation for the BHNS system, in the ST gravity (green) and GR (blue).

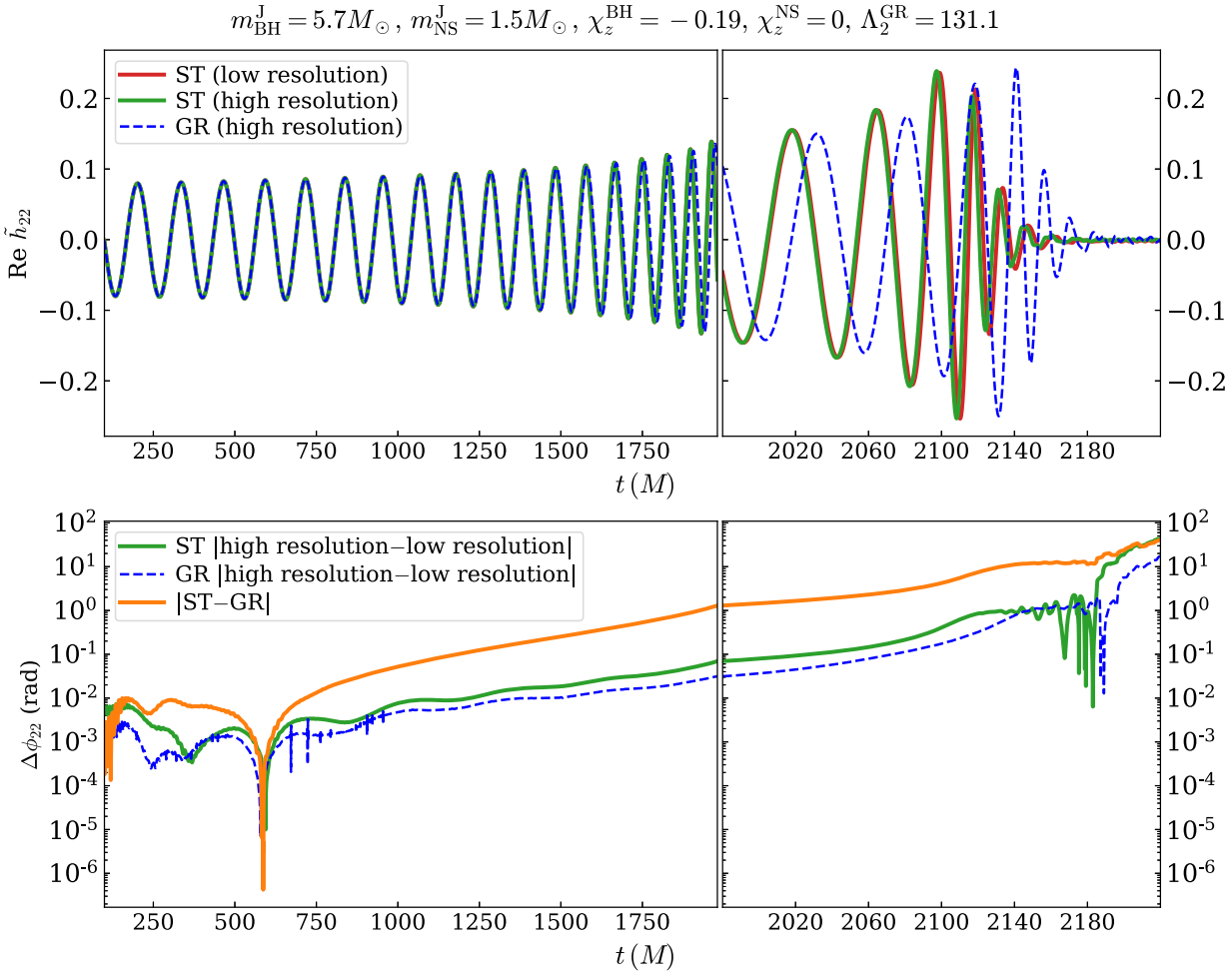

FIG. 9. Upper panel: The ST waveforms with a low (in red) and high (in green) resolution. They are compared to the GR waveform (in blue). Lower panel: the phase difference between the GR and ST waveforms (in orange). For reference, the numerical resolution differences of the GR and the ST waveform are also presented in blue and green, respectively. In addition, we summarize some of the binary parameters in the title.

capture the effect of scalar radiation well above the numerical resolution difference, even though our simulations are less accurate than other recent BHNS SpEC simulations [136], as discussed in Sec. IV A.

D. Comparing to post-Newtonian theory

We now carry out quantitative comparisons between the simulated GW waveforms and existing PN waveform predictions in ST. As pointed out in Refs. [43,45], the relative size of the leading scalar dipolar radiation and leading tensor quadrupolar radiation is given by

$$\frac{\mathcal{F}_{\rm nd}}{\mathcal{F}_{\rm d}}=\left(\frac{24}{5\zeta\mathcal{S}_-^2}\right)x, \tag{27}$$

with $\mathcal{F}$ being energy flux. In our simulation, we find the factor above is greater than 25, i.e. quadrupolar radiation dominates, so we are in the quadrupole-driven regime [43].

We first consider the gravitational modes $\tilde{h}_{lm}$, whose PN expressions read [43]

$$\tilde{h}_{lm}=2\tilde{G}(1-\zeta)\eta x\sqrt{\frac{16\pi}{5}}\hat{H}_{lm}e^{-im\phi}, \tag{28}$$

where $\eta=m_{\rm BH}^{\rm J}m_{\rm NS}^{\rm J}/(m_{\rm BH}^{\rm J}+m_{\rm NS}^{\rm J})^2$ is the symmetric mass ratio, $x=(\tilde{G}M\alpha\Omega_{\rm orb})^{2/3}$ is the PN expansion parameter, $\Omega_{\rm orb}$ is the orbital frequency, and we give ϕ below. We summarize the definition of ST parameters $\tilde{G},\zeta,\alpha$ in Table II. In Eq. (28), comparing with Eq. (65) of Ref. [43], we removed an overall factor M/r which is already divided out in Eq. (14a). The expressions for $\hat{H}_{lm}$ are long and they can be found in Eq. (67) of Ref. [43]. Because the dipolar scalar radiation starts 1PN earlier than the leading quadrupolar gravitational radiation, the inspiral is separated into two parts: dipolar (D) or nondipolar (ND). The phase factor ϕ reads

TABLE II. Summary of PN parameters used for ST gravity. We have used the fact that a BH's scalar charge vanishes: $\alpha_{\rm BH} = 0$, and thus $s_{\rm BH} = 1/2$ following Eq. (31). Note that α is not to be confused with the scalar charge $\alpha_{\rm NS}$.

ω_0	$\tilde{G}$	ζ	α	$\mathcal{S}_-$	$\mathcal{S}_+$	ξ
$\frac{1-3\alpha_0^2}{2\alpha_0^2}$	$\frac{1+\alpha_0^2}{\phi_0}$	$\frac{\alpha_0^2}{1+\alpha_0^2}$	$\frac{1}{1+\alpha_0^2}$	$-\alpha^{1/2} s_{\rm NS}$	$\alpha^{1/2}(1-s_{\rm NS})$	$1+\frac{\zeta \mathcal{S}_+^2}{6}$

$$\phi = \phi_{\rm nd} + \phi_{\rm d}, \tag{29a}$$

$$\phi_{\rm nd} = -\frac{x^{-5/2}}{32\eta\xi}\left[1 + \frac{5}{3}\rho_2^{\rm nd} x + \frac{5}{2}\rho_3^{\rm nd} x^{3/2} + 5\rho_4^{\rm nd} x^2 + \frac{5}{2}\rho_3^{\rm spin} x^{3/2} + 5\rho_4^{\rm spin} x^2\right], \tag{29b}$$

$$\phi_{\rm d} = \frac{25\mathcal{S}_-^2 \zeta x^{-7/2}}{5376\eta\xi^2}\left[1 + \frac{7}{5}\rho_2^{\rm d} x + \frac{7}{4}\rho_3^{\rm d} x^{3/2} + \frac{7}{3}\rho_4^{\rm d} x^2\right], \tag{29c}$$

with the coefficients $\rho_i^{\rm nd/d}$'s being listed in Eq. (B10) of Ref. [43]. The ST parameters ξ and $\mathcal{S}_\pm$ are defined in Table II, and we see that all of them depend on the sensitivity of the NS

$$s_{\rm NS} = \left(\frac{d\ln m_{\rm NS}^{\rm I}}{d\ln\phi}\right)_{\phi_0}. \tag{30}$$

The relationship between $s_{\rm NS}$ and the scalar charge $\alpha_{\rm NS}$ reads [43]

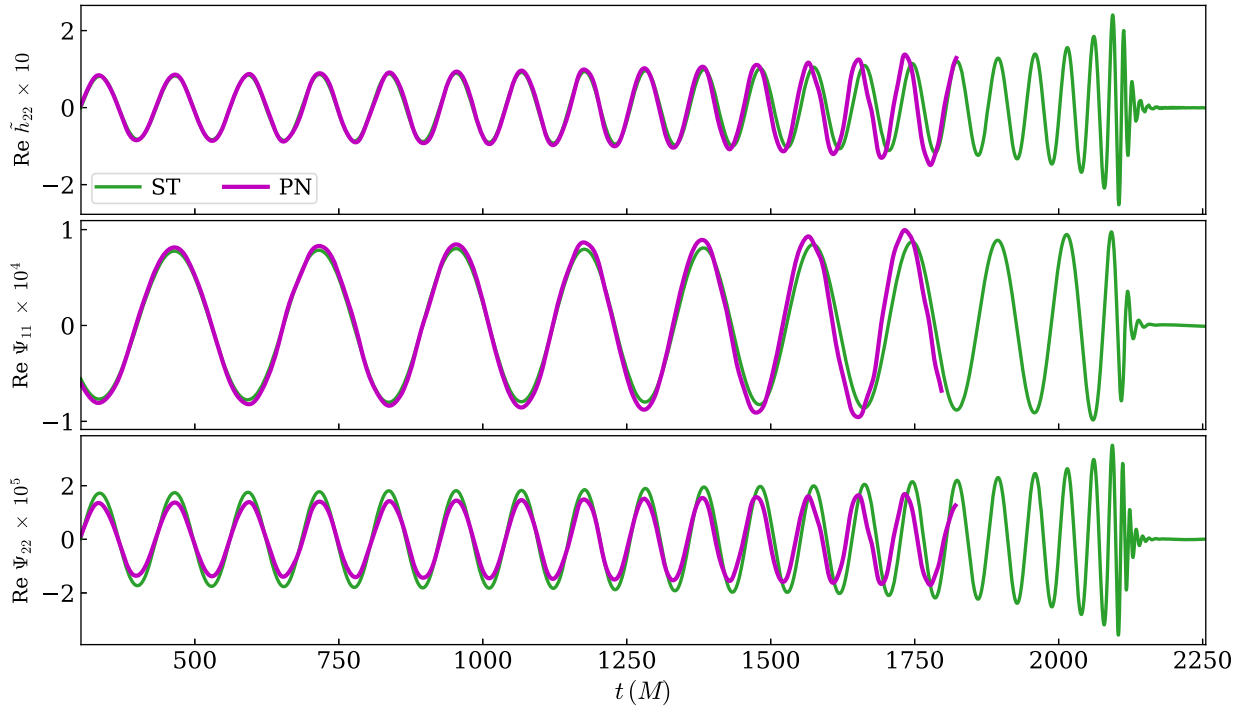

(a) ST

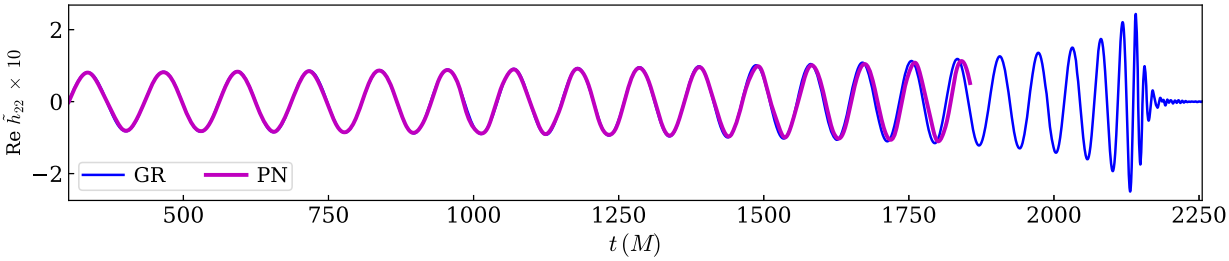

(b) GR

FIG. 10. Comparing the numerical waveforms (in green and blue) to the PN model (in magenta). (a) shows the ST tensor harmonic $\tilde{h}_{22}$ (top) and the scalar modes Ψ_{11} (middle) and Ψ_{22} (bottom). Note that the modes Ψ_{lm} are defined in Eq. (36). (b) provides the GR tensor harmonic $\tilde{h}_{22}$.

$$s_{\rm NS} = \frac{1}{2} - \frac{\alpha_{\rm NS}}{2\alpha_0}, \tag{31}$$

where α_0 is the ST parameter defined in Eq. (18). Equation (29) is controlled by the quadrupolar radiation, while Eq. (29c) is controlled by the dipolar radiation starting at −1PN. Spin effects are not considered in Ref. [43]; here we simply add the spin contributions in GR, leading to the second line in Eq. (29b), and we leave the relevant ST corrections for future studies. The expressions of $\rho_i^{\rm spin}$'s can be found in Eq. (4.16) of Ref. [139],

$$\rho_3^{\rm spin} = \frac{1}{12}\sum_{i=1,2}\chi_i(\hat{\boldsymbol{L}}_N\cdot\hat{\boldsymbol{s}}_i)\left(113\frac{m_i^2}{M^2}+75\eta\right), \tag{32}$$

$$\rho_4^{\rm spin} = \frac{1}{48}\eta\chi_1\chi_2[247(\hat{\boldsymbol{s}}_1\cdot\hat{\boldsymbol{s}}_2)-721(\hat{\boldsymbol{L}}_N\cdot\hat{\boldsymbol{s}}_1)(\hat{\boldsymbol{L}}_N\cdot\hat{\boldsymbol{s}}_2)], \tag{33}$$

where $\hat{\boldsymbol{L}}_N$ and $\hat{\boldsymbol{s}}_i$ stand for the unit vector along the orbital angular momentum and the individual spin $\boldsymbol{s}_i$. Furthermore, we note that tidal effects are ignored in Eq. (29a), which formally enter into the phase evolution at 5PN order [132]. This is reasonable for this study, as the system's mass-weighted tidal deformability $\tilde{\Lambda}_2^{\rm GR} \sim 2.95$ is very small and it has little impact on the binary dynamics, as shown in Fig. 4. In the top panel of Fig. 10(a), we compare the ST numerical waveform $\tilde{h}_{22}$ to the PN prediction, finding good agreement until $\sim 500M$ before the merger. For reference, we also plot the GR waveform $\tilde{h}_{22}$ and the corresponding PN prediction in Fig. 10(b). Additionally, in Appendix D, we present a more detailed comparison by demonstrating the hierarchical contributions of each PN term.

We then compare the scalar modes ψ_{lm} extracted from our simulation with predictions from PN. The PN prediction for the (l, m) harmonic of the transverse breathing mode Ψ [see Eq. (11)] is given by [45]

$$\Psi_{lm} = 2i\tilde{G}\zeta\sqrt{\alpha}\mathcal{S}_-\eta\sqrt{x}\sqrt{\frac{8\pi}{3}}\hat{\Phi}_{lm}e^{-im\phi}, \tag{34}$$

where the expression of $\hat{\Phi}_{lm}$ can be found in Eq. (6.10) of Ref. [45]; and Ψ_{lm} is defined in parallel with Eq. (14b):

$$r\Psi/M = \sum_{l,m} Y_{lm}(\iota,\varphi)\Psi_{lm}. \tag{35}$$

Here Ψ_{lm} is related to our numerical extracted scalar mode ψ_{lm} [Eq. (14b)] via

$$\Psi_{lm} = -4\sqrt{\pi}\alpha_0\psi_{lm}, \tag{36}$$

where Eq. (17) has been used. We compare our numerical scalar modes Ψ_{11} and Ψ_{22} to the PN predictions in the middle and bottom rows of Fig. 10(a), and refer to Appendix C for other (subdominant) modes. Similar to $\tilde{h}_{22}$, the PN predictions for the ψ_{lm} phase evolution are accurate until $\sim 500M$ before merger; however, their amplitudes do not match as accurately as their phases.

V. WAVEFORM DISTINGUISHABILITY

We have discussed features of the BHNSs in GR and ST. Then in this section, we investigate how our numerical simulations can help place constraints on ST theory with GW200115 and future BHNS observations. Specifically, here we focus on whether a ST waveform can be distinguished from a GR waveform. We estimate this by computing the mismatch $\mathcal{M}$ between the two waveforms, defined in Eq. (21). Note that in Eq. (22), we used a flat noise curve for simplicity, namely assuming an idealized detector.

We first compute the mismatch between the GR and ST waveform $\tilde{h}_{22}$ presented in Fig. 9 and find $\mathcal{M} = 0.38$. Since the error in our simulations is larger than other BHNS SpEC simulations (see discussions around Figs. 4 and 9), we terminate the integration in Eq. (22) at the peak of the ST waveform $(t_2 = 2102M)$ to avoid the ringdown region. One criterion for the distinguishability of two waveforms reads [140–144]

$$\mathcal{M} > \frac{D}{2\rho^2}, \tag{37}$$

where $D = 5$ is the number of free intrinsic parameters (chirp mass, mass ratio, spin magnitudes on both compact objects, and tidal deformability) of our nonprecessing systems, and ρ is the signal-to-noise ratio (SNR). After inserting the numbers, we find $\rho > 2.56$ is needed to distinguish ST from GR. Such a low SNR threshold is not surprising for this specific case with extreme scalarization and an idealized detector, given the significant dephasing between the two waveforms shown in Fig. 9. For more moderate ST parameters and more realistic detectors, the deviation is not expected to be as large, and we leave this exploration for future work.

The subsequent question to consider is the extent to which tidal effects within GR can replicate the ST waveform. To explore this question, we employ an effective-one-body (EOB) model known as `SEOBNRv4T` [145,146]. This model includes tidal effects and is characterized by tidal deformability coefficients Λ_l in its tidal sector, with $l = 2$ being the focus in this case. To generate the `SEOBNRv4T` waveforms with varying $\Lambda_2^{\rm GR}$, we utilize LALSuite [147]. Figure 11 showcases the mismatch of these waveforms with the ST waveform $\tilde{h}_{22}$ as a function of $\Lambda_2^{\rm GR}$ while fixing other intrinsic parameters at their NR values. The mismatch first decreases when $\Lambda_2^{\rm GR}$ is small, and the best match $\mathcal{M} \sim 0.023$ happens at $\Lambda_2^{\rm GR} \sim 4000$. As a comparison, we repeat the same calculation for the

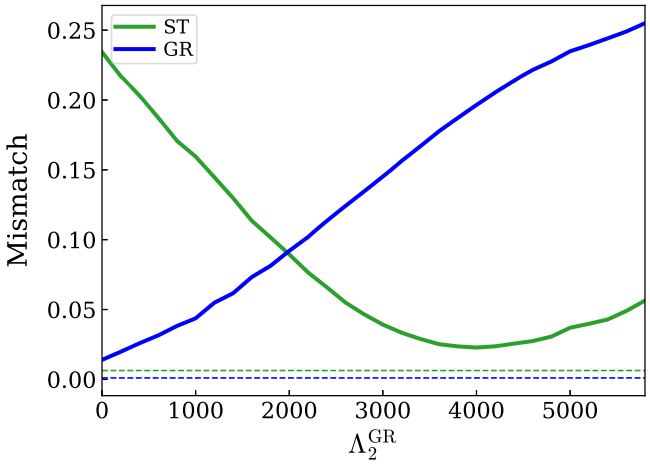

FIG. 11. The mismatch of the SEOBNRv4T model with the ST waveform (green) and the GR result (blue), as a function of tidal deformability $\Lambda_2^{\rm GR}$. For the sake of comparison, we also compute the mismatch between two resolutions for ST (green dashed line) and GR (blue dashed line).

mismatch between the SEOBNRv4T model and the GR waveform. The result is shown as the blue curve in Fig. 11, and we can see the mismatch grows monotonically with $\Lambda_2^{\rm GR}$ (recall the tidal effect is negligible in the GR simulation). To better understand the feature, in Fig. 12 we provide the SEOBNRv4T waveforms with a variety of $\Lambda_2^{\rm GR}$, ranging from 0 to 6000. In particular, we mark the best-fit waveform ($\Lambda_2^{\rm GR} = 4000$) with black crosses. With increasing $\Lambda_2^{\rm GR}$, we see the tidal waveforms gradually shift backward in time, because the tidal effect accelerates the evolution and shortens the length of waveforms. This behavior is similar to the effect of the scalar field and dipole radiation. Notably, as $\Lambda_2^{\rm GR}$ approaches 4000, the last two wave cycles of the SEOBNRv4T waveforms (at $t \sim 2075M$) align more closely with ST's phase evolution, resulting in a smaller mismatch. Further increasing $\Lambda_2^{\rm GR}$ beyond this point causes the tidal waveforms to deviate again from the ST waveform. Therefore, the mismatch in Fig. 11 bounces back.

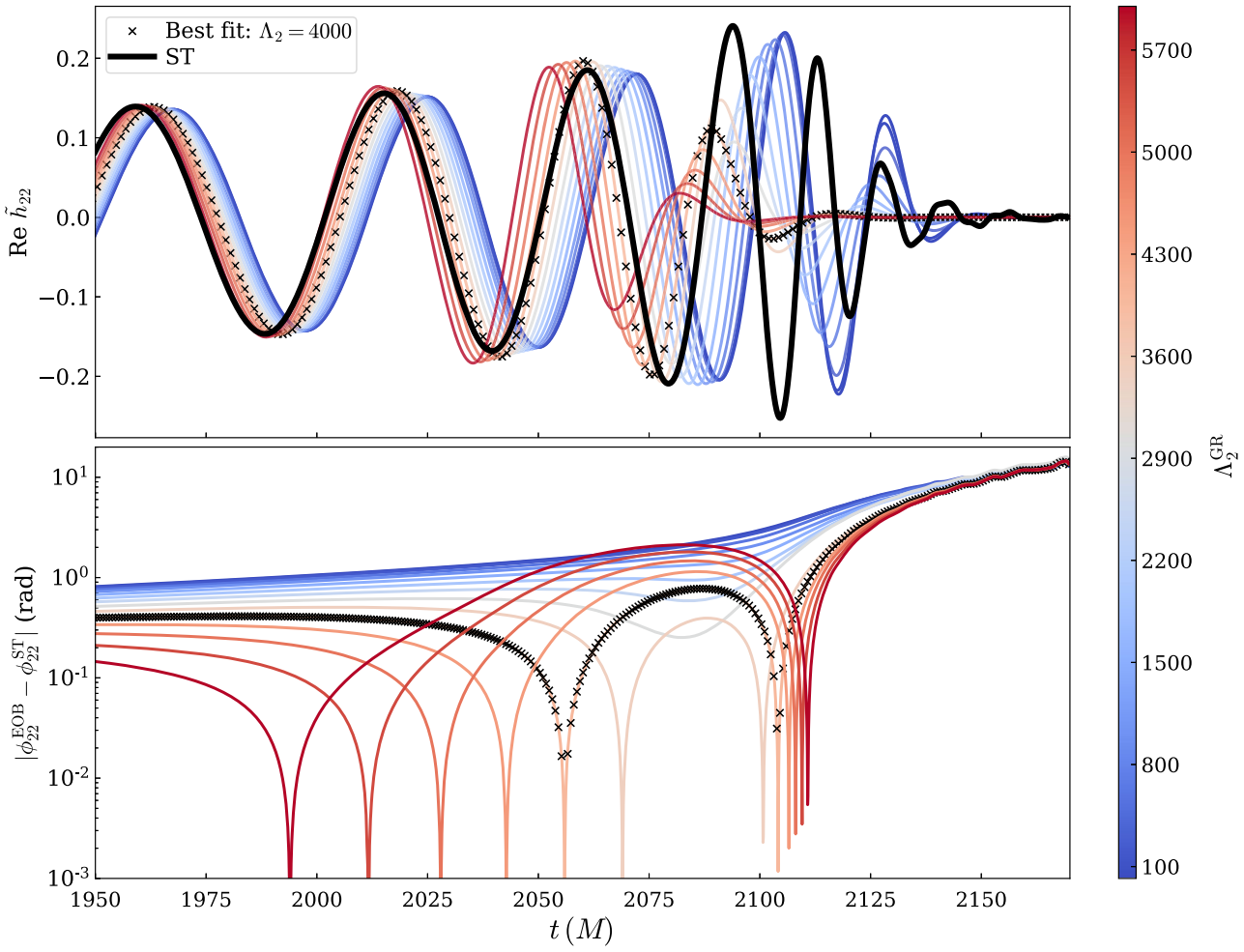

FIG. 12. Comparing the ST waveform (black) with the SEOBNRv4T model, with a variety of $\Lambda_2^{\rm GR}$, ranging from 0 to 6000. The minimum mismatch $\mathcal{M} \sim 0.023$ happens at $\Lambda_2^{\rm GR} \sim 4000$.

Our preliminary mismatch comparison shows that both the tidal and scalar sectors could produce similar and potentially degenerate imprints in GWs given the length of our simulations (∼12 cycles before the merger). A limitation of our analysis is that the NR waveforms are relatively short and lacked low-frequency components—the dipole radiation appears at −1PN whereas the tidal effect at 5PN. A longer waveform with a broader frequency span may break the degeneracy. A more comprehensive analysis is therefore necessary to fully characterize these features using longer waveforms with a broader frequency span and Bayesian parameter estimation. We leave this exploration to future research.

VI. CONCLUSION

In this paper, we numerically simulate a fully relativistic BHNS binary system in ST theory, chosen to be consistent with GW200115 [89]. To maximize the effect of spontaneous scalarization, we set the ST parameters (β_0, α_0) to be at the boundary of known constraints from other observations [9]: $(-4.5, -3.5 \times 10^{-3})$. In addition, we select a soft EOS for the NS so that it can generate a large scalar charge, as summarized in Table I. Following Refs. [134,135], we construct the initial data without including the scalar sector. Instead, the scalar field dynamically grows during the first $\sim 50M$, and quickly approaches the desired value predicted by the isolated NS solver.

We evolve the BHNS system with both GR and ST. For the GR binary, we find the soft EOS results in GW emissions that are nearly identical to those of a BBH system with the same spins and mass ratio. In contrast, the ST binary exhibits dominant dipolar radiation due to spontaneous scalarization, with the spatial distribution of the scalar field ψ matching the dipolar emission pattern throughout the computational domain. As a result of this additional dipolar radiation, the ST binary evolves faster than its GR counterpart, and the ST binary reaches its peak amplitude one whole GW cycle earlier than the GR counterpart. We also compare our waveforms, including the tensor mode $\tilde{h}_{22}$ and scalar breathing modes $\Psi_{11,22}$, with existing PN waveform predictions in ST [43,45,139], and find reasonable agreement up to $\sim 500M$ before the merger. Finally, we compute the mismatch between our ST waveform and the `SEOBNRv4T` model as a function of tidal deformability $\Lambda_2^{\rm GR}$. We find the ST waveform could be partially mimicked by a GR tidal waveform with a large $\Lambda_2^{\rm GR} \sim 4000$, due to the tidal effect accelerating the evolution of the binary.

Throughout the analysis, we pick optimal choices for the EOS and the ST theory parameters in order to produce a significant scalarization effect, and thus strong dipolar radiation. Under this idealized scenario, we find that the GR and ST waveforms should be distinguishable for SNRs above 2.56. To fully understand observational prospects of constraining ST theory using BHNS systems, future work should explore a wider range of EOSs and more moderate ST parameters. Specifically, the scalar field's ability to alter the properties of NSs, such as compactness and radius, may play a crucial role in determining whether the NSs are disrupted or not [148], potentially leading to rich phenomena in the corresponding GW and even electromagnetic emissions for ST binary systems.

Our mismatch tests using the `SEOBNRv4T` model and the GR waveforms indicate that the ST sector might be partially degenerate with tidal effects during the late inspiral stage (excluding low-frequency regime), which can lead to parameter estimation biases. Here we restrict ourselves to a single degree of freedom: $\Lambda_2^{\rm GR}$, while holding other parameters such as mass ratio and spins constant. A possible avenue for future work is to carry out a more systematic full Bayesian parameter estimation to better account for these degeneracies.

Finally, our waveforms are obtained at null infinity through extrapolation following Refs. [114,118–120], with the Python package SCRI [121,122]. The method is an approximate approach that relies on the asymptotic behavior of several fields given by the peeling theorem [149]. While this approximate approach captures linear signals, it does not accurately capture nonlinear features such as the memory effect [150–155]. The more correct Cauchy-characteristic extraction (CCE) [115,116] method would be required to fully account for these effects. Therefore, another future avenue could be to evolve the coupled metric-scalar system using a CCE framework adapted to ST, and investigate the memory effect in ST gravity [150–153,156–158].

ACKNOWLEDGMENTS

We thank Laura Bernard, David Trestini, Luc Blanchet, Noah Sennet, Sylvain Marsat, and Alessandra Buonanno for sharing Mathematica notebooks with PN expressions. We thank David Trestini, Hector Silva, and Dongze Sun for useful discussions. V. V. acknowledges funding from the European Union's Horizon 2020 research and innovation program under the Marie Skłodowska-Curie Grant Agreement No. 896869. V. V. was supported by a Klarman Fellowship at Cornell. V. V. is a Marie Curie Fellow. L. C. S. was partially supported by NSF CAREER Award No. PHY-2047382. S. M. and M. S. acknowledge funding from the Sherman Fairchild Foundation and by NSF Grants No. PHY-2011961, No. PHY-2011968, and No. OAC-2209655 at Caltech.

APPENDIX A: THE TWO-GRID METHOD AND TRANSFORMATIONS

In the Einstein frame, we adopt the $3+1$ decomposition of the metric [159]

$$ds^2 = -\bar{\alpha}^2 dt^2 + \bar{\gamma}_{ij}(dx^i + \bar{\beta}^i dt)(dx^j + \bar{\beta}^j dt), \quad \text{(A1)}$$

where $\bar{\alpha}$, $\bar{\beta}^i$, $\bar{\gamma}_{ij}$ are the lapse, shift, and 3-metric in the Einstein frame. They, their spatial derivatives, and the extrinsic curvature K_{ij} are transformed to the Jordan frame via:

$$\begin{aligned}
&\alpha = \frac{1}{\sqrt{\phi}}\bar{\alpha}, \quad \beta^i = \bar{\beta}^i, \quad \gamma_{ij} = \frac{1}{\phi}\bar{\gamma}_{ij}, \quad \gamma^{ij} = \phi\bar{\gamma}^{ij},\\
&K_{ij} = \frac{1}{\sqrt{\phi}}\left(\bar{K}_{ij} + \frac{\bar{\gamma}_{ij}}{2}\frac{d\log\phi}{d\psi}\bar{n}^k\partial_k\psi\right),\\
&\partial_k\alpha = \frac{1}{\sqrt{\phi}}\left(\partial_k\bar{\alpha} - \frac{\bar{\alpha}}{2}\frac{d\log\phi}{d\psi}\partial_k\psi\right),\\
&\partial_k\beta^i = \partial_k\bar{\beta}^i,\\
&\partial_k\gamma^{ij} = \phi\left(\partial_k\bar{\gamma}^{ij} + \bar{\gamma}^{ij}\frac{d\log\phi}{d\psi}\partial_k\psi\right),
\end{aligned} \tag{A2}$$

where the future-directed unit timelike normal is given by

$$\bar{n}^a = \bar{\alpha}^{-1}(\partial_t^a - \bar{\beta}^i\partial_i^a). \tag{A3}$$

On the other hand, the transformation of the stress-energy tensor $\bar{T}^{ab}$ can be established from its definition

$$\bar{T}^{ab} = \frac{2}{\sqrt{-\bar{g}}}\frac{\delta S_M}{\delta\bar{g}_{ab}}. \tag{A4}$$

After inserting

$$\begin{aligned}
\bar{g}_{ab} &= \phi g_{ab},\\
\sqrt{-\bar{g}} &= \phi^2\sqrt{-g},
\end{aligned} \tag{A5}$$

into Eq. (A4), we obtain

$$\bar{T}^{ab} = \frac{2}{\sqrt{-\bar{g}}}\frac{\delta S_M}{\delta\bar{g}_{ab}} = \frac{1}{\phi^3}\frac{2}{\sqrt{-g}}\frac{\delta S_M}{\delta g_{ab}} = \frac{1}{\phi^3}T^{ab}, \tag{A6}$$

which leads to $\bar{T}_{ab} = T_{ab}/\phi$.

APPENDIX B: STRUCTURE OF NEUTRON STARS IN ST GRAVITY

Following Ref. [125], the Einstein-frame metric of an isolated, nonspinning NS can be written as

$$d\bar{s}^2 = -e^{\nu(r)}dt^2 + \frac{dr^2}{1-2\mu(r)/r} + r^2(d\theta^2 + \sin^2\theta d\phi^2). \tag{B1}$$

Then the equations of motion are given by

$$\mu' = 4\pi r^2A^4(\rho_0 h - P) + \frac{1}{2}r(r-2\mu)\varphi^2, \tag{B2a}$$

$$\nu' = 8\pi\frac{r^2A^4P}{r-2\mu} + r\varphi^2 + \frac{2\mu}{r(r-2\mu)}, \tag{B2b}$$

$$\psi' = \frac{1}{\sqrt{4\pi}}\varphi, \tag{B2c}$$

$$\begin{aligned}
\varphi' = {}& 4\pi\frac{rA^4}{r-2\mu}[(\alpha_0 + \beta_0\sqrt{4\pi}\psi)(\rho_0 h - 4P)\\
&+ r\varphi(\rho_0 h - 2P)] - \frac{2(r-\mu)}{r(r-2\mu)}\varphi,
\end{aligned} \tag{B2d}$$

$$P' = -\rho_0 h\left[\frac{1}{2}\nu' + (\alpha_0 + \beta_0\sqrt{4\pi}\psi)\varphi\right], \tag{B2e}$$

with $A = \phi^{-1/2}$. Note that P, ρ_0, and h are in the Jordan frame. The system of coupled ordinary differential equations can be solved as an initial value problem integrating out from $r = \epsilon > 0$. The asymptotic expansion of the solution near the stellar center $r \to 0$ is

$$\begin{aligned}
\mu(r) &\sim \frac{1}{3!}\mu_3 r^3,\\
\nu(r) &\sim \frac{1}{2!}\nu_2 r^2,\\
\varphi(r) &\sim \varphi_1 r,\\
\psi(r) &\sim \psi_c + \frac{1}{2!}\frac{1}{\sqrt{4\pi}}\varphi_1 r^2,\\
P(r) &\sim P_c + \frac{1}{2!}P_2 r^2,
\end{aligned} \tag{B3}$$

where

$$\begin{aligned}
\mu_3 &= 8\pi A_c^4(\rho_c h_c - P_c),\\
\nu_2 &= 8\pi A_c^4 P_c + \frac{\mu_3}{3},\\
\varphi_1 &= \frac{4\pi}{3}A_c^4(\alpha_0 + \beta_0\sqrt{4\pi}\psi_c)(\rho_c h_c - 4P_c),\\
P_2 &= -\rho_c h_c\left[\frac{1}{2}\nu_2 + (\alpha_0 + \beta_0\sqrt{4\pi}\psi_c)\varphi_1\right].
\end{aligned} \tag{B4}$$

We start the integration of Eq. (B2) at $\epsilon = 10^{-7}R_{\rm ST}^{\rm E}$ away from the stellar center, and terminate at the stellar surface. From surface values, we obtain the scalar charge of the NS via [125]

$$\alpha_{\rm NS} = \left.\frac{2\varphi}{\nu'}\right|_{\rm surf}, \tag{B5}$$

and the Einstein-frame mass

$$\begin{aligned}
m_{\rm NS}^{\rm E} = {}& \exp\left[-\frac{1}{\sqrt{1+\alpha_{\rm NS}^2}}\operatorname{arctanh}\left(\frac{\sqrt{1+\alpha_{\rm NS}^2}}{1+2/(r\nu')}\right)\right]\\
&\times\left.\frac{r^2\nu'}{2}\left(1-\frac{2\mu}{r}\right)^{1/2}\right|_{\rm surf}.
\end{aligned} \tag{B6}$$

It is related to the Jordan-frame mass through [32]

$$m^{\mathrm{J}}_{\mathrm{NS}} = m^{\mathrm{E}}_{\mathrm{NS}}(1 + \alpha_0 \alpha_{\mathrm{NS}}). \tag{B7}$$

For a Newtonian star, Eq. (B2) reduce to

$$\mu' = 4\pi r^2 A^4(\psi_\infty)\rho_0, \tag{B8a}$$

$$P' = -\frac{\rho_0 \mu}{r^2}, \tag{B8b}$$

where the scalar field ψ decouples from the matter and it becomes constant across the star. Here we denote its (background) value as ψ_∞. Next we can compute the baryonic mass m^B and the Einstein-frame mass $m^{\mathrm{E}}_{\mathrm{NS}}$ of the NS:

$$m^B = A^3(\psi_\infty) \int 4\pi \rho_0 r^2 dr, \tag{B9a}$$

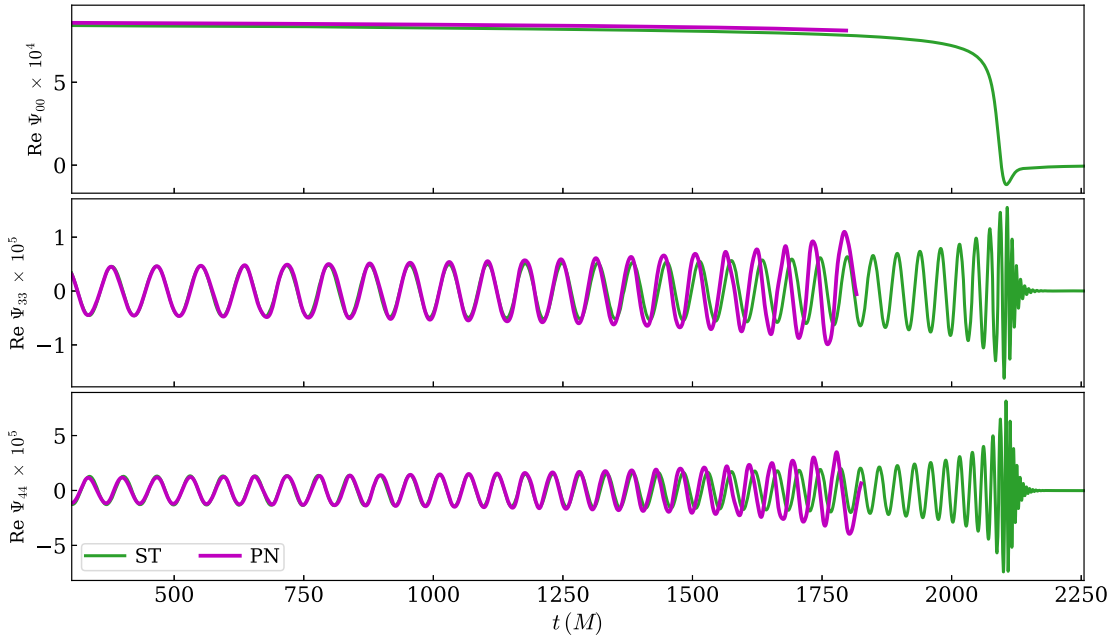

(a) Scalar modes

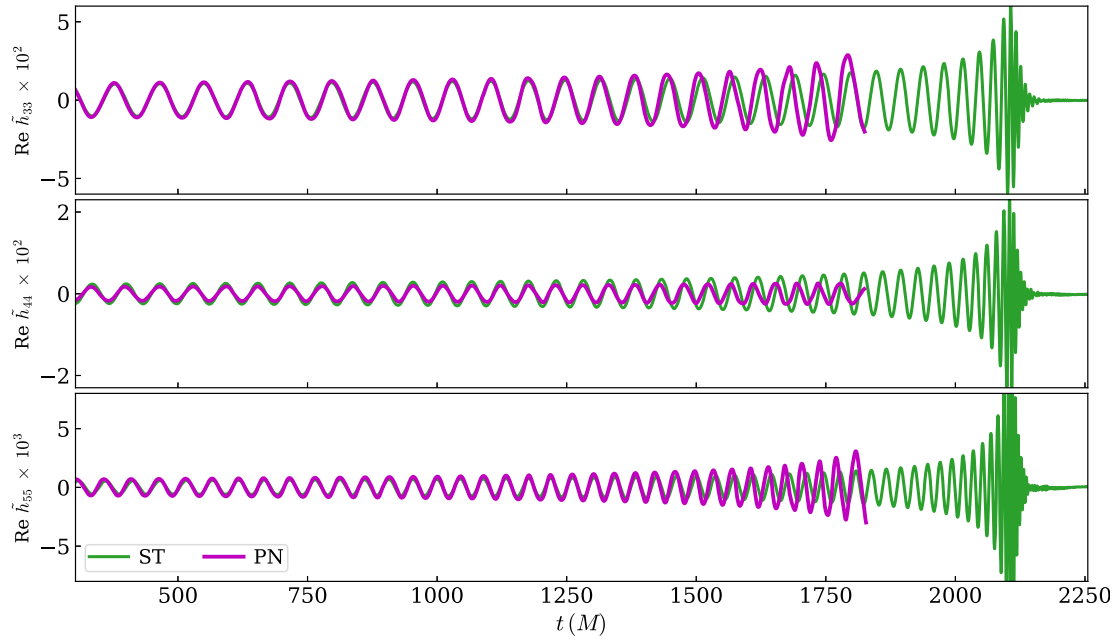

(b) Tensor modes

FIG. 13. Same as Fig. 10, some other scalar and tensor modes. Note that the modes Ψ_{lm} are defined in Eq. (36).

TABLE III. Summary of all the PN orders in the amplitude of $\tilde{h}_{22}$, Ψ_{11}, and Ψ_{22}.

Modes	Available PN orders	References
$\tilde{h}_{22}$	0PN, 1PN, 1.5PN, 2PN	Equation (67) of [43]
Ψ_{11}	−0.5PN, 0.5PN, 1PN	Equation (6.10b) of [45]
Ψ_{22}	0PN, 1PN	Equation (6.10c) of [45]

$$m^{\mathrm{E}}_{\mathrm{NS}} = A^4(\psi_\infty)\int 4\pi\rho_0 r^2 dr = m^B A(\psi_\infty). \tag{B9b}$$

As shown in Refs. [32,125], the scalar charge can be computed alternatively through

$$\alpha_{\mathrm{NS}} = \frac{1}{\sqrt{4\pi}}\left(\frac{\partial \ln m^{\mathrm{E}}_{\mathrm{NS}}}{\partial\psi_\infty}\right)_{m^B}. \tag{B10}$$

After plugging Eq. (B9b), we obtain $\alpha_{\mathrm{NS}} = \alpha_0$ [see Eq. (17)].

APPENDIX C: SOME OTHER SCALAR AND TENSOR MODES

Figure 13 displays additional scalar and tensor modes of the ST simulation.

APPENDIX D: HIERARCHICAL CONTRIBUTIONS FROM PN TERMS

In Fig. 10, we compared the ST waveforms with the existing PN predictions that include all the PN orders. Exploring the hierarchical contributions of each PN term is also an interesting aspect to investigate. Here we focus on the amplitude of $\tilde{h}_{22}$ [Eq. (28)], Ψ_{11} and Ψ_{22} [Eq. (34)], which are controlled by $\hat{H}_{lm}$ and $\hat{\Phi}_{lm}$ [43]. Table III outlines all the relevant PN orders of $\tilde{h}_{22}$, Ψ_{11}, and Ψ_{22}. Our convention considers the leading Newtonian quadrupole approximation in GR, namely $\mathcal{O}(1)$ in $\hat{H}_{lm}$, as 0PN. In contrast, the prefactor of Eq. (34) is 0.5PN $(x^{1/2})$ lower than that of Eq. (28), thus the term $\mathcal{O}(1)$ in $\hat{\Phi}_{lm}$ represents −0.5PN.

We depict the size of each PN term as solid lines with different colors in Fig. 14. For reference, the dashed lines represent the ones with all the PN contributions. The lowest PN order contributes the most, while higher PN corrections improve consistency. The amplitude of Ψ_{22} is the least accurate. Higher PN terms may be needed to improve the agreement with numerical simulations.

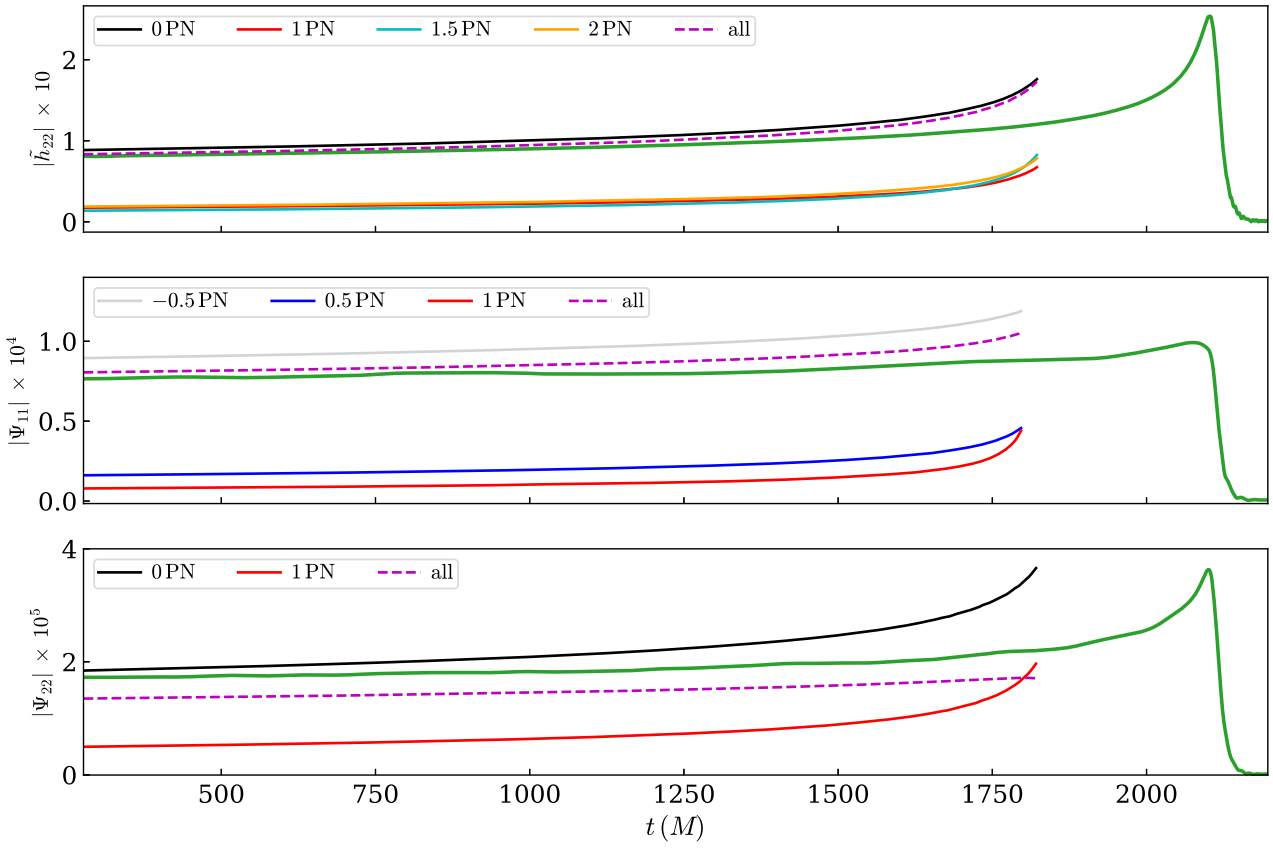

FIG. 14. Contributions of individual PN orders to the amplitude of $\tilde{h}_{22}$ (top), Ψ_{11} (middle), and Ψ_{22} (bottom). It is important to note that a PN curve only includes contributions from the specific PN order, not lower PN orders. The magenta dashed curves refer to the ones that include all the PN terms.

[1] B. P. Abbott *et al.* (LIGO Scientific, Virgo Collaborations), Phys. Rev. X **6**, 041015 (2016); **8**, 039903(E) (2018).
[2] B. P. Abbott *et al.* (LIGO Scientific, Virgo Collaborations), Phys. Rev. X **9**, 031040 (2019).
[3] R. Abbott *et al.* (LIGO Scientific, Virgo Collaborations), Phys. Rev. X **11**, 021053 (2021).
[4] R. Abbott *et al.* (LIGO Scientific, Virgo, KAGRA Collaborations), arXiv:2111.03606.
[5] B. P. Abbott *et al.* (LIGO Scientific, Virgo Collaborations), Phys. Rev. Lett. **116**, 221101 (2016); **121**, 129902(E) (2018).
[6] C. M. Will, Living Rev. Relativity **17**, 4 (2014).
[7] N. Yunes and X. Siemens, Living Rev. Relativity **16**, 9 (2013).
[8] N. Yunes, K. Yagi, and F. Pretorius, Phys. Rev. D **94**, 084002 (2016).
[9] E. Berti *et al.*, Classical Quantum Gravity **32**, 243001 (2015).
[10] B. P. Abbott *et al.* (LIGO Scientific, Virgo Collaborations), Phys. Rev. Lett. **123**, 011102 (2019).
[11] A. Krolak, K. D. Kokkotas, and G. Schaefer, Phys. Rev. D **52**, 2089 (1995).
[12] K. Yagi and T. Tanaka, Prog. Theor. Phys. **123**, 1069 (2010).
[13] S. Ma and N. Yunes, Phys. Rev. D **100**, 124032 (2019).
[14] Z. Carson, B. C. Seymour, and K. Yagi, Classical Quantum Gravity **37**, 065008 (2020).
[15] L. Sampson, N. Yunes, N. Cornish, M. Ponce, E. Barausse, A. Klein, C. Palenzuela, and L. Lehner, Phys. Rev. D **90**, 124091 (2014).
[16] P. D. Scharre and C. M. Will, Phys. Rev. D **65**, 042002 (2002).
[17] C. M. Will and N. Yunes, Classical Quantum Gravity **21**, 4367 (2004).
[18] E. Berti, A. Buonanno, and C. M. Will, Classical Quantum Gravity **22**, S943 (2005).
[19] E. Berti, A. Buonanno, and C. M. Will, Phys. Rev. D **71**, 084025 (2005).
[20] K. Yagi and T. Tanaka, Phys. Rev. D **81**, 064008 (2010); **81**, 109902(E) (2010).
[21] K. G. Arun, Classical Quantum Gravity **29**, 075011 (2012).
[22] V. Cardoso, S. Chakrabarti, P. Pani, E. Berti, and L. Gualtieri, Phys. Rev. Lett. **107**, 241101 (2011).
[23] N. Yunes, P. Pani, and V. Cardoso, Phys. Rev. D **85**, 102003 (2012).
[24] E. Berti, L. Gualtieri, M. Horbatsch, and J. Alsing, Phys. Rev. D **85**, 122005 (2012).
[25] S. Tuna, K. I. Ünlütürk, and F. M. Ramazanoğlu, Phys. Rev. D **105**, 124070 (2022).
[26] P. Jordan, *Schwerkraft Und Weltall: Grundlagen Der Theoretischen Kosmologie* (Die Wissenschaft, 1955).
[27] M. Fierz, Helv. Phys. Acta **29**, 128 (1956).
[28] C. Brans and R. H. Dicke, Phys. Rev. **124**, 925 (1961).
[29] C. H. Brans, in *Gravitation and Cosmology*, American Institute of Physics Conference Series Vol. 1083, edited by A. Herrera-Aguilar, F. S. G. Murillo, U. N. Gómez, and I. Quiros (Lavoisier, Paris, 2008), pp. 34–46.
[30] P. G. Bergmann, Int. J. Theor. Phys. **1**, 25 (1968).
[31] R. V. Wagoner, Phys. Rev. D **1**, 3209 (1970).
[32] T. Damour and G. Esposito-Farese, Classical Quantum Gravity **9**, 2093 (1992).
[33] C. M. Will and H. W. Zaglauer, Astrophys. J. **346**, 366 (1989).
[34] D. M. Eardley, Astrophys. J. Lett. **196**, L59 (1975).
[35] T. Damour and G. Esposito-Farese, Phys. Rev. D **53**, 5541 (1996).
[36] S. Mirshekari and C. M. Will, Phys. Rev. D **87**, 084070 (2013).
[37] L. Bernard, Phys. Rev. D **98**, 044004 (2018).
[38] L. Bernard, Phys. Rev. D **99**, 044047 (2019).
[39] C. M. Will, Astrophys. J. **214**, 826 (1977).
[40] M. Brunetti, E. Coccia, V. Fafone, and F. Fucito, Phys. Rev. D **59**, 044027 (1999).
[41] C. M. Will, Phys. Rev. D **50**, 6058 (1994).
[42] R. N. Lang, Phys. Rev. D **89**, 084014 (2014).
[43] N. Sennett, S. Marsat, and A. Buonanno, Phys. Rev. D **94**, 084003 (2016).
[44] R. N. Lang, Phys. Rev. D **91**, 084027 (2015).
[45] L. Bernard, L. Blanchet, and D. Trestini, J. Cosmol. Astropart. Phys. 08 (2022) 008.
[46] M. Saijo, H.-a. Shinkai, and K.-i. Maeda, Phys. Rev. D **56**, 785 (1997).
[47] T. Damour and J. H. Taylor, Phys. Rev. D **45**, 1840 (1992).
[48] T. Damour and G. Esposito-Farese, Phys. Rev. D **54**, 1474 (1996).
[49] T. Damour and G. Esposito-Farese, Phys. Rev. D **58**, 042001 (1998).
[50] J. H. Taylor, A. Wolszczan, T. Damour, and J. M. Weisberg, Nature (London) **355**, 132 (1992).
[51] D. Psaltis, arXiv:astro-ph/0501234.
[52] P. C. C. Freire, N. Wex, G. Esposito-Farese, J. P. W. Verbiest, M. Bailes, B. A. Jacoby, M. Kramer, I. H. Stairs, J. Antoniadis, and G. H. Janssen, Mon. Not. R. Astron. Soc. **423**, 3328 (2012).
[53] L. Shao, N. Sennett, A. Buonanno, M. Kramer, and N. Wex, Phys. Rev. X **7**, 041025 (2017).
[54] D. Anderson, P. Freire, and N. Yunes, Classical Quantum Gravity **36**, 225009 (2019).
[55] A. M. Archibald, N. V. Gusinskaia, J. W. T. Hessels, A. T. Deller, D. L. Kaplan, D. R. Lorimer, R. S. Lynch, S. M. Ransom, and I. H. Stairs, Nature (London) **559**, 73 (2018).
[56] J. Antoniadis *et al.*, Science **340**, 6131 (2013).
[57] J. Zhao, L. Shao, Z. Cao, and B.-Q. Ma, Phys. Rev. D **100**, 064034 (2019).
[58] J. Zhao, P. C. C. Freire, M. Kramer, L. Shao, and N. Wex, Classical Quantum Gravity **39**, 11LT01 (2022).
[59] J. M. Gerard and Y. Wiaux, Phys. Rev. D **66**, 024040 (2002).
[60] I. H. Stairs, Living Rev. Relativity **6**, 5 (2003).
[61] L. Shao and N. Wex, Sci. China Phys. Mech. Astron. **59**, 699501 (2016).
[62] M. Kramer, Int. J. Mod. Phys. D **25**, 1630029 (2016).
[63] N. Wex, arXiv:1402.5594.
[64] G. Esposito-Farese, in *10th Marcel Grossmann Meeting on Recent Developments in Theoretical and Experimental General Relativity, Gravitation and Relativistic Field Theories (MG X MMIII)* (World Scientific Publication, Singapore, 2004), pp. 647–666, arXiv:gr-qc/0402007.

[65] M. Kramer and N. Wex, Classical Quantum Gravity **26**, 073001 (2009).
[66] T. Damour, in *6th SIGRAV Graduate School in Contemporary Relativity and Gravitational Physics: A Century from Einstein Relativity: Probing Gravity Theories in Binary Systems* (2007), arXiv:0704.0749.
[67] R. A. Hulse and J. H. Taylor, Astrophys. J. Lett. **195**, L51 (1975).
[68] M. W. Horbatsch and C. P. Burgess, Classical Quantum Gravity **29**, 245004 (2012).
[69] T. Damour and G. Esposito-Farese, Phys. Rev. Lett. **70**, 2220 (1993).
[70] D. Anderson and N. Yunes, Classical Quantum Gravity **36**, 165003 (2019).
[71] K. S. Thorne and J. J. Dykla, Astrophys. J. Lett. **166**, L35 (1971).
[72] T. P. Sotiriou and V. Faraoni, Phys. Rev. Lett. **108**, 081103 (2012).
[73] S. W. Hawking, Commun. Math. Phys. **25**, 167 (1972).
[74] J. Healy, T. Bode, R. Haas, E. Pazos, P. Laguna, D. Shoemaker, and N. Yunes, Classical Quantum Gravity **29**, 232002 (2012).
[75] E. Barausse, C. Palenzuela, M. Ponce, and L. Lehner, Phys. Rev. D **87**, 081506 (2013).
[76] M. Shibata, K. Taniguchi, H. Okawa, and A. Buonanno, Phys. Rev. D **89**, 084005 (2014).
[77] K. Taniguchi, M. Shibata, and A. Buonanno, Phys. Rev. D **91**, 024033 (2015).
[78] C. Palenzuela, E. Barausse, M. Ponce, and L. Lehner, Phys. Rev. D **89**, 044024 (2014).
[79] N. Sennett and A. Buonanno, Phys. Rev. D **93**, 124004 (2016).
[80] N. Sennett, L. Shao, and J. Steinhoff, Phys. Rev. D **96**, 084019 (2017).
[81] H. Sotani, Phys. Rev. D **86**, 124036 (2012).
[82] F. M. Ramazanoğlu and F. Pretorius, Phys. Rev. D **93**, 064005 (2016).
[83] R. Rosca-Mead, U. Sperhake, C. J. Moore, M. Agathos, D. Gerosa, and C. D. Ott, Phys. Rev. D **102**, 044010 (2020).
[84] D. D. Doneva, F. M. Ramazanoğlu, H. O. Silva, T. P. Sotiriou, and S. S. Yazadjiev, arXiv:2211.01766.
[85] T. Harada, Prog. Theor. Phys. **98**, 359 (1997).
[86] T. Harada, Phys. Rev. D **57**, 4802 (1998).
[87] J. Aasi *et al.* (LIGO Scientific Collaborations), Classical Quantum Gravity **32**, 074001 (2015).
[88] F. Acernese *et al.* (Virgo Collaborations), Classical Quantum Gravity **32**, 024001 (2015).
[89] R. Abbott *et al.* (LIGO Scientific, KAGRA, Virgo Collaborations), Astrophys. J. Lett. **915**, L5 (2021).
[90] B. P. Abbott *et al.* (KAGRA, LIGO Scientific, Virgo Collaborations), Living Rev. Relativity **21**, 3 (2018).
[91] M. Punturo *et al.*, Classical Quantum Gravity **27**, 194002 (2010).
[92] S. Hild *et al.*, Classical Quantum Gravity **28**, 094013 (2011).
[93] B. P. Abbott *et al.* (LIGO Scientific Collaboration), Classical Quantum Gravity **34**, 044001 (2017).
[94] D. Reitze *et al.*, Bull. Am. Astron. Soc. **51**, 035 (2019).
[95] M. Khalil, N. Sennett, J. Steinhoff, and A. Buonanno, Phys. Rev. D **100**, 124013 (2019).
[96] M. Khalil, R. F. P. Mendes, N. Ortiz, and J. Steinhoff, Phys. Rev. D **106**, 104016 (2022).
[97] L. Bernard, Phys. Rev. D **101**, 021501 (2020).
[98] T. Harada, T. Chiba, K.-i. Nakao, and T. Nakamura, Phys. Rev. D **55**, 2024 (1997).
[99] M. A. Scheel, S. L. Shapiro, and S. A. Teukolsky, Phys. Rev. D **51**, 4236 (1995).
[100] M. A. Scheel, S. L. Shapiro, and S. A. Teukolsky, Phys. Rev. D **51**, 4208 (1995).
[101] M. Shibata, K.-i. Nakao, and T. Nakamura, Phys. Rev. D **50**, 7304 (1994).
[102] T. Matsuda and H. Nariai, Prog. Theor. Phys. **49**, 1195 (1973).
[103] J. Novak, Phys. Rev. D **57**, 4789 (1998).
[104] M. Bezares, R. Aguilera-Miret, L. ter Haar, M. Crisostomi, C. Palenzuela, and E. Barausse, Phys. Rev. Lett. **128**, 091103 (2022).
[105] M. Salgado, Classical Quantum Gravity **23**, 4719 (2006).
[106] M. Salgado, D. Martinez-del Rio, M. Alcubierre, and D. Nunez, Phys. Rev. D **77**, 104010 (2008).
[107] The Spectral Einstein Code, http://www.black-holes.org/SpEC.html.
[108] Simulating eXtreme Spacetimes, http://www.black-holes.org/.
[109] L. Lindblom, M. A. Scheel, L. E. Kidder, R. Owen, and O. Rinne, Classical Quantum Gravity **23**, S447 (2006).
[110] M. Holst, L. Lindblom, R. Owen, H. P. Pfeiffer, M. A. Scheel, and L. E. Kidder, Phys. Rev. D **70**, 084017 (2004).
[111] M. A. Scheel, A. L. Erickcek, L. M. Burko, L. E. Kidder, H. P. Pfeiffer, and S. A. Teukolsky, Phys. Rev. D **69**, 104006 (2004).
[112] M. D. Duez, F. Foucart, L. E. Kidder, H. P. Pfeiffer, M. A. Scheel, and S. A. Teukolsky, Phys. Rev. D **78**, 104015 (2008).
[113] M. Boyle and A. H. Mroue, Phys. Rev. D **80**, 124045 (2009).
[114] D. A. B. Iozzo, M. Boyle, N. Deppe, J. Moxon, M. A. Scheel, L. E. Kidder, H. P. Pfeiffer, and S. A. Teukolsky, Phys. Rev. D **103**, 024039 (2021).
[115] J. Moxon, M. A. Scheel, and S. A. Teukolsky, Phys. Rev. D **102**, 044052 (2020).
[116] J. Moxon, M. A. Scheel, S. A. Teukolsky, N. Deppe, N. Fischer, F. Hébert, L. E. Kidder, and W. Throwe, Phys. Rev. D **107**, 064013 (2023).
[117] E. Poisson and C. M. Will, *Gravity: Newtonian, Post-Newtonian, Relativistic* (Cambridge University Press, Cambridge, England, 2014).
[118] M. Boyle, Phys. Rev. D **87**, 104006 (2013).
[119] M. Boyle, L. E. Kidder, S. Ossokine, and H. P. Pfeiffer, arXiv:1409.4431.
[120] M. Boyle, Phys. Rev. D **93**, 084031 (2016).
[121] M. Boyle, SCRI, https://github.com/moble/scri.
[122] M. Boyle, D. Iozzo, and L. C. Stein, moble/SCRI: v1.2 (2020).
[123] A. Buonanno, L. E. Kidder, A. H. Mroue, H. P. Pfeiffer, and A. Taracchini, Phys. Rev. D **83**, 104034 (2011).
[124] K. Yagi and M. Stepniczka, Phys. Rev. D **104**, 044017 (2021).
[125] T. Damour and G. Esposito-Farèse, Phys. Rev. Lett. **70**, 2220 (1993).

[126] D. Anderson, N. Yunes, and E. Barausse, Phys. Rev. D **94**, 104064 (2016).
[127] P. J. Steinhardt and C. M. Will, Phys. Rev. D **52**, 628 (1995).
[128] B. Boisseau, G. Esposito-Farese, D. Polarski, and A. A. Starobinsky, Phys. Rev. Lett. **85**, 2236 (2000).
[129] B. Bertotti, L. Iess, and P. Tortora, Nature (London) **425**, 374 (2003).
[130] F. Foucart, M. D. Duez, A. Gudinas, F. Hebert, L. E. Kidder, H. P. Pfeiffer, and M. A. Scheel, Phys. Rev. D **100**, 104048 (2019).
[131] T. Hinderer, Astrophys. J. **677**, 1216 (2008).
[132] E. E. Flanagan and T. Hinderer, Phys. Rev. D **77**, 021502 (2008).
[133] B. Szilágyi, Int. J. Mod. Phys. D **23**, 1430014 (2014).
[134] F. Foucart, L. E. Kidder, H. P. Pfeiffer, and S. A. Teukolsky, Phys. Rev. D **77**, 124051 (2008).
[135] N. Tacik, F. Foucart, H. P. Pfeiffer, C. Muhlberger, L. E. Kidder, M. A. Scheel, and B. Szilágyi, Classical Quantum Gravity **33**, 225012 (2016).
[136] F. Foucart *et al.*, Phys. Rev. D **103**, 064007 (2021).
[137] L. Wade, J. D. E. Creighton, E. Ochsner, B. D. Lackey, B. F. Farr, T. B. Littenberg, and V. Raymond, Phys. Rev. D **89**, 103012 (2014).
[138] V. Varma, S. E. Field, M. A. Scheel, J. Blackman, D. Gerosa, L. C. Stein, L. E. Kidder, and H. P. Pfeiffer, Phys. Rev. Res. **1**, 033015 (2019).
[139] L. E. Kidder, Phys. Rev. D **52**, 821 (1995).
[140] E. E. Flanagan and S. A. Hughes, Phys. Rev. D **57**, 4566 (1998).
[141] L. Lindblom, B. J. Owen, and D. A. Brown, Phys. Rev. D **78**, 124020 (2008).
[142] S. T. McWilliams, B. J. Kelly, and J. G. Baker, Phys. Rev. D **82**, 024014 (2010).
[143] K. Chatziioannou, A. Klein, N. Yunes, and N. Cornish, Phys. Rev. D **95**, 104004 (2017).
[144] M. Boyle *et al.*, Classical Quantum Gravity **36**, 195006 (2019).
[145] T. Hinderer *et al.*, Phys. Rev. Lett. **116**, 181101 (2016).
[146] J. Steinhoff, T. Hinderer, A. Buonanno, and A. Taracchini, Phys. Rev. D **94**, 104028 (2016).
[147] LIGO Scientific Collaboration, LIGO Algorithm Library—LALSuite, free software (GPL) (2018), 10.7935/GT1W-FZ16.
[148] F. Foucart, T. Hinderer, and S. Nissanke, Phys. Rev. D **98**, 081501 (2018).
[149] E. Newman and R. Penrose, J. Math. Phys. (N.Y.) **3**, 566 (1962).
[150] S. M. Du and A. Nishizawa, Phys. Rev. D **94**, 104063 (2016).
[151] K. Koyama, Phys. Rev. D **102**, 021502 (2020).
[152] S. Hou and Z.-H. Zhu, J. High Energy Phys. 01 (2021) 083.
[153] A. Seraj, J. High Energy Phys. 05 (2021) 283.
[154] K. Mitman, J. Moxon, M. A. Scheel, S. A. Teukolsky, M. Boyle, N. Deppe, L. E. Kidder, and W. Throwe, Phys. Rev. D **102**, 104007 (2020).
[155] K. Mitman *et al.*, Phys. Rev. D **103**, 024031 (2021).
[156] S. Tahura, D. A. Nichols, A. Saffer, L. C. Stein, and K. Yagi, Phys. Rev. D **103**, 104026 (2021).
[157] S. Tahura, D. A. Nichols, and K. Yagi, Phys. Rev. D **104**, 104010 (2021).
[158] L. Heisenberg, N. Yunes, and J. Zosso, arXiv:2303.02021.
[159] T. W. Baumgarte and S. L. Shapiro, *Numerical Relativity: Solving Einstein's Equations on the Computer* (Cambridge University Press, Cambridge, England, 2010).